# Genesis of the Gentio Metagranitoid: Post-Collisional High-K Plutonism within the Mineiro Belt, São Francisco Craton, Brazil

**Marize M. da Silva** ⓘD*[1], **Ciro A. Ávila**[1,2], **Felipe M. Tavares**[3], **Natali S. Barbosa**[3], **Wilson Teixeira**[4]

1. *Programa de Pós-graduação em Geologia, Universidade Federal do Rio de Janeiro, 21.949-900 Rio de Janeiro RJ, Brazil*
2. *Museu Nacional, Universidade Federal do Rio de Janeiro, 20940-040 Rio de Janeiro RJ, Brazil*
3. *Serviço Geológico do Brasil, Divisão de Geologia Econômica, 22290-255 Rio de Janeiro, Brazil*
4. *Instituto de Geociências, Universidade Federal da Bahia, 40170-110 Salvador BA, Brazil*
ⓘD Marize M. da Silva: https://orcid.org/0000-0001-8879-0323

**ABSTRACT:** The Gentio metagranitoid presents equigranular and porphyritic facies, modal composition ranging from tonalite to monzogranite with calculated $T_{Zr}$<800 °C for most samples. Its mineralogy is dominated by quartz and feldspar (77% to 95%), biotite is the only mafic mineral present (2% to 18%) and, titanite, zircon, apatite, allanite are important accessory phases. These rocks range from metaluminous to weakly peraluminous, and have large variation in major and trace elements, and high alkali contents (>6 wt.%). Zircon analyses by LA-ICP-MS and SHRIMP yielded a concordia age of 2 119±10 Ma for the porphyritic facies and an upper intercept age of 2 111±15 Ma for the equigranular facies. The whole-rock Sm-Nd $T_{DM}$ ages vary from 2.4 to 2.8 Ga with $\varepsilon_{Nd}(2.1)$ values between -0.7 and -5.3, indicating crustal derivation from distinct and/or heterogeneous protoliths. Field observations indicate that the Gentio metagranitoid was formed through different pulses of magma. Individual batches were subject to little or even no fractionation process after its emplacement. Although the Gentio metagranitoid crosscuts metamafic and metaultramafic rocks akin to an oceanic arc setting, this pluton is likely originated by partial melting of a more evolved quartz-feldspathic crustal igneous rock in a post-collisional environment, after the accretion of the arcs from the Mineiro belt and rocks of the Mantiqueira Complex.
**KEY WORDS:** high-K granites, Mineiro belt, post-collisional, São Francisco Craton, U-Pb geochronology.

## 0 INTRODUCTION

Granitic rocks can be generated by partial melting of different types of lithologies, and depending upon $P$-$T$-$a_{H_2O}$ conditions during partial melting the same rock can lead to the production of a wide variety of melt composition (e.g., Patiño Douce and McCarthy, 1998; Roberts and Clemens, 1993; Holtz and Johannes, 1991; Conrad et al., 1988). These rocks represent an advanced stage in the magmatic crustal evolution and their study is fundamental to the understanding of continental crust formation, growth, and differentiation. According to Roberts and Clemens (1993) 35% to 40% of the total post-Archean granitoid exhibits high-K calc-alkaline affinity. The binary diagram $K_2O$ vs. $SiO_2$ (Peccerillo and Taylor, 1976) can be used to categorize them into calc-alkaline, high-K calc-alkaline, or shoshonitic suites. Experimental data have demonstrated that the $K_2O$ content is mainly dependent on the parental rock composition and the amount of water available during partial melting (Roberts and Clemens, 1993; Beard and Lofgren, 1991; Conrad et al., 1988). The generation of high-K calc-alkaline plutons seems to require the presence of crustal source material and thus, they may be present in a continental arc setting (Andes type) and collisional orogens.

The youngest magmatic episodes within the Mineiro belt—São Francisco Craton—dated between 2.14 and 2.10 Ga generated a significant volume of high-K calc-alkaline granitoids like the Gentio metagranitoid studied here. Granitoids correspond to at least 65% of the total currently known area of the Mineiro belt and the larger plutons are classified as high-K calc-alkaline and peraluminous rocks. Therefore, their study is crucial for the comprehension of the magmatic history and tectonic evolution of this belt. In this sense, we present here the first detailed investigation on one of the major batholiths occurring in the southern block of the Mineiro belt: the Gentio metagranitoid.

## 1 REGIONAL GEOLOGY

The Mineiro belt is located on the southern border of the São Francisco Craton (Fig. 1), bounded by the Archean polycyclic basement in the north and by the Paleoproterozoic Mantiqueira Complex in the southeast (Alkmim and Teixeira, 2017; Heilbron et al., 2010). It is partially covered by the Meso–Neoproterozoic São João del Rei, Carandaí, and Andrelândia

Silva, M. M., Ávila, C. A., Tavares, F. M., et al., 2021. Genesis of the Gentio Metagranitoid: Post-Collisional High-K Plutonism within the Mineiro Belt, São Francisco Craton, Brazil. *Journal of Earth Science*, 32(6): 1374–1396. https://doi.org/10.1007/s12583-021-1469-0. http://en.earth-science.net
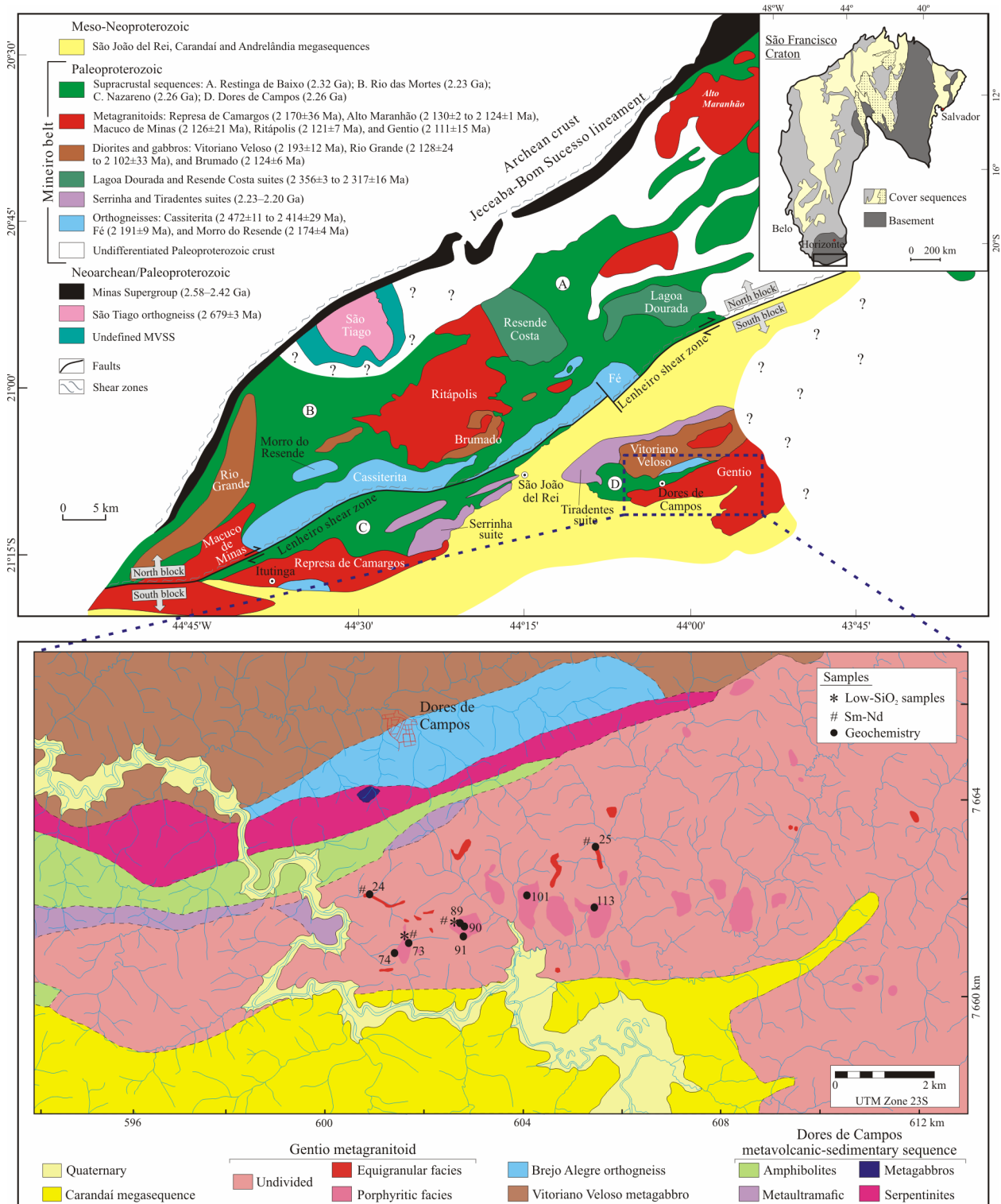
**Figure 1.** Geologic framework of the Mineiro belt located in the southern portion of the São Francisco Craton (adapted from Ávila et al., 2014, 2010). The representation of the different facies is based on the predominance of each in an outcrop scale. The dots represent the locations where samples were collected for chemical analysis. Symbols # showing the location where samples were collected for Sm-Nd analysis and * the locations where samples from the low-SiO2 were collected.

metasedimentary units (Ribeiro et al., 2013). Ávila et al. (2014) subdivided this belt into two blocks—northern and southern (Table 1), limited by the Lenheiro shear zone (Fig. 1). From a tectonic perspective, the northern block includes three arc-type plutonic associations (Cassiterita 2.47–2.41 Ga, Resende Costa 2.36–2.33 Ga, and Ritápolis 2.19–2.10 Ga) and three metavolcanic-

sedimentary sequences (Restinga de Baixo 2.32 Ga, Congonhas-Itaverava <2.35 Ga, and Rio das Mortes 2.23–2.20 Ga). On the other hand, the southern block (Table 1) hosts the Serrinha arc, formed by the Serrinha and Tiradentes suites (2.25–2.20 Ga) and two metavolcanic-sedimentary sequences of Rhyacian age (Nazareno 2.27 Ga, and Dores de Campos 2.26 Ga).

**Table 1**  Summary of the tectonic subdivision of the Mineiro belt

| Blocks | Tectonic unit | Units | Lithotypes | U-Pb age/isotopic constraints | Geochemistry | Tectonic | References |
|---|---|---|---|---|---|---|---|
| Southern | Serrinha arc | Nazareno metavolcanic-sedimentary sequence | Abundant metaultramafic rock with amphibolite and minor phyllite | 2 267±4 and 2 223±4 Ma; Sm-Nd $T_{DM}$ (2.7–2.8 Ga); $\varepsilon_{Nd}(t)$ (-0.1 to -1.45); $^{87}Sr/^{86}Sr_{(t)}$ (0.702–0.704) | MORB affinity (amphibolites) | Oceanic arc | Ávila et al. (2012) |
| | | Dores de Campos metavolcanic-sedimentary sequence | Amphibolites and metaultramafic rocks | 2 255±51 Ma; Sm-Nd $T_{DM}$ (2.2–2.5 Ga); $\varepsilon_{Nd}(t)$ (+1.2 to +3.6) | Island arc tholeiite (amphibolites) | Oceanic arc | Ávila et al. (2012) |
| | | Serrinha Suite | Metavolcanic, metasubvolcanic and metaplutonic rocks | 2 227±22 to 2 211±22 Ma; Sm-Nd $T_{DM}$ (2.6–2.3 Ga); $\varepsilon_{Nd}(t)$ (-0.53 to +1.8); $^{87}Sr/^{86}Sr_{(t)}$ (0.704–0.706) | Calc-alkaline, slightly metaluminous to peraluminous. | Oceanic arc | Ávila et al. (2010) |
| | | Tiradentes Suite | Metavolcanic and metasubvolcanic rocks | 2 217±23 to 2 204±11 Ma; Sm-Nd $T_{DM}$ (2.4–2.3 Ga); $\varepsilon_{Nd}(t)$ (+1.1 to +2.3); $^{87}Sr/^{86}Sr_{(t)}$ (0.701 8–0.703 2) | Calc-alkaline, slightly metaluminous to peraluminous. | Oceanic arc | Ávila et al. (2014) |
| | | Tiradentes Station metasedimentary sequence | Phyllites, quartzites, gondites, metawackes and metadiamictites | (Quartzite) <2 088±12 Ma | | Back-arc | Ávila et al. (2014) |
| Northern | Cassiterita arc | Cassiterita orthogneiss | Tonalitic and granodioritic orthogneiss | 2 472±11 to 2 414±29 Ma; Sm-Nd $T_{DM}$ (2.5–2.4 Ga); $\varepsilon_{Nd}(t)$ (+5.2 to +1.3); $^{87}Sr/^{86}Sr_{(t)}$ (0.700–0.702) | TTG affinity, metaluminous to slightly peraluminous | Oceanic arc | Barbosa et al. (2019) |
| | Resende Costa arc | Lagoa Dourada and Resende Costa suites | Tonalitic and granodioritic orthogneiss | 2 351±48 to 2 317±16 Ma; Sm-Nd $T_{DM}$ (2.5–2.4 Ga); $\varepsilon_{Nd}(t)$ (+1.1 to +2.1) | TTG affinity, slightly metaluminous to peraluminous | Oceanic arc | Seixas et al. (2012); Teixeira et al. (2015); Moreira et al. (2018) |
| | | Congonhas-Itaverava metavolcanic-sedimentary sequence | Metagraywackes, phyllite, marbles, BIFs, metabasalts | (Metagraywacke) 2 349±14 Ma; $\varepsilon_{Nd}(t)$ (+2.7 to +3.5) in metabasalt | Metabasalts: High-Fe and high-Mg tholeiite, | Foreland (metagraywacke) MORB (metabasalts) | Teixeira et al. (2015) |
| | | Restinga de Baixo metavolcanic-sedimentary sequence | Pyroxene-bearing amphibolite, phyllites, and metaultramafic rocks | (Amphibolite) 2 317±16 Ma; Sm-Nd $T_{DM}$ (2.4–2.7 Ga); $\varepsilon_{Nd}(t)$ (+4 to +7) | MORB affinity (amphibolites) | Oceanic arc | Teixeira et al. (2015) |
| | Ritápolis arc | Plutonic rocks | Metadiorites, metatonalites, metagranodiorites and metagranites | 2 143±10 to 2 106±5 Ma; Sm-Nd $T_{DM}$ (2.5–2.4 Ga); $\varepsilon_{Nd}(t)$ (-4.7 to -7.7) | Calc-alkaline, metaluminous to peraluminous. | Continental arc | Barbosa et al. (2015); Cardoso et al. (2019) |
| | | | Tonalitic to granitic orthogneiss | 2 191±9 to 2 174±4; Sm-Nd $T_{DM}$ (2.7–2.5 Ga); $\varepsilon_{Nd}(t)$ (-3.3 to -0.3); $^{87}Sr/^{86}Sr_{(t)}$ (0.702–0.750) | Calc-alkaline, metaluminous to peraluminous | Continental arc | Ávila et al. (2006b); Teixeira et al. (2008); Vasconcelos et al. (2017) |
| | | Rio das Mortes metavolcanic-sedimentary sequence | Phyllites, amphibolites, and minor metaultramafic rocks | 2 231±15 and 2 202±11 Ma; $\varepsilon_{Nd}(t)$ (+0.1 to -1.5) | MORB affinity (amphibolites) | Oceanic arc | Ávila et al. (2012) |

The Gentio metagranitoid (the focus of this study) crops out in the southern block of the Mineiro belt and intrudes amphibolitic and metaultramafic rocks of the Dores de Campos metavolcanic-sedimentary sequence (Fig. 1). This sequence comprises amphibolites, with crystallization age of 2 255±51 Ma, associated with metagabbros, serpentinites, chlorite-serpentine-tremolite schists, and rare metasedimentary rocks, represented by phyllites and scarce gondite (Ávila et al., 2012). It was interpreted by Ávila et al. (2014) as a large Paleoproterozoic seafloor where the volcanic-subvolcanic rocks of the Tiradentes and Serrinha suites were formed—in an intra-oceanic arc setting. The metavolcanic-sedimentary sequence is also intruded by plutonic bodies such as the Dores de Campos metaquartz-diorite (2 199±7 Ma, Ávila et al., 2006a), the Brejo Alegre tonalitic orthogneiss (2 166±5 Ma, Silva et al., 2020), and the Vitoriano Veloso metagabbro.

The Dores de Campos metavolcanic-sedimentary sequence is limited to the north by metamafic andesites, metadacites, metagranophyres, and intrusive metatonalites of the Tiradentes Suite (Ávila et al., 2014), in the southeast by the rocks of the Carandaí megasequence and, in the south by the Gentio metagranitoid (Fig. 1).

The Ribeira belt was formed during the Neoproterozoic orogeny of western Gondwana. Its Paleoproterozoic basement, exposed on the Occidental terrain, corresponds to the extension of the São Francisco paleocontinent and is represented by the Mantiqueira Complex which consists of felsic orthogneisses of calc-alkaline affinity associated with layers of amphibolites and metaultramafic rocks (Alkmim and Teixeira, 2017; Heilbron et al., 2017, 2010). This complex was interpreted as formed in a Cordilleran-type active margin of the Archean paleocontinent (2.70–2.60 Ga) with a substantial generation of magmatic rocks in a time interval of 2.22–2.05 Ga (Heilbron et al., 2017, 2010; Noce et al., 2007; Duarte et al., 2004). Unlike the Mineiro belt, the Mantiqueira Complex was deeply reworked during the Neoproterozoic/Cambrian Brasiliano orogeny (Heilbron et al., 2017, 2010).

The Mineiro belt is intruded by a diversity of Paleoproterozoic plutonic bodies with variable compositions, associated with at least five magmatic pulses with different ages: (i) 2.47–2.41 Ga; (ii) 2.35–2.31 Ga; (iii) 2.23–2.20 Ga; (iv) 2.19–2.17 Ga; (v) 2.14–2.10 Ga. The two oldest intervals occur only in the northern block and are represented by orthogneisses of TTG composition associated with the formation of the Cassiterita and Resende Costa arcs (Barbosa et al., 2019; Teixeira et al., 2015; Seixas et al., 2012). The third interval is found only in the southern block and it is related to the Serrinha arc whose rocks show calc-alkaline affinity (Ávila et al., 2014, 2010). The fourth and fifth intervals occur all over the Mineiro belt and are represented by calc-alkaline to high-K calc-alkaline plutons such as the Ritápolis, and the Represa de Camargos metagranitoids interpreted as having been formed in a continental arc setting (Barbosa et al., 2015) and by the rocks of the Alto Maranhão Suite that show chemical compositions similar to sanukitoids (Seixas et al., 2013) (Fig. 1).

## 2  ANALYTICAL METHODS

Twenty-one samples of the Gentio metagranitoid were selected for geochemical analyses after petrographic characterization (Tables 2 and 3). The selected samples were crushed and then ground below 74 μm in an agate disc mill. Geochemistry analyses for major and trace elements were carried out at the Acme Analytical Laboratories Ltd. (Vancouver, Canada). Major elements (21 samples) were measured by inductively coupled plasma emission spectrometry (ICP-ES) while trace elements and REE (20 samples) were measured by an inductively coupled plasma-mass spectrometer (ICP-MS).

Chemical compositions of biotite and plagioclase were determined from polished thin sections using a JEOL JXA-8230 electron microprobe analyzer (EMPA) with five wavelength dispersive X-ray spectrometers (WDS) and an energy dispersive X-ray spectrometer (EDS) at the Federal University of Rio de Janeiro. Minerals were analyzed with a focused beam with a current of 20 nA, an acceleration voltage of 15 kV, and counting time ranging from 5 to 10 s. Results are presented in the ESM, Supplementary Dataset A and B with the respective structural formulas and calculated end-members. Calibration of the electron microprobe was based on natural mineral standards: plagioclase ($An_{65}$), Sonora, Mexico; Great Sitkin Island; sanidine, Hohenfels, Germany; microcline, unknown location (Smithsonian Standart); plagioclase (labradorite), Lake Country; and biotite, unknown location (Astimex Scientific Limited Standards).

Additional plagioclase analyses were also carried out using an FEI Quanta 400 scanning electron microscope (SEM) coupled to a Bruker Nano Quantax 800 energy dispersive spectrometer (EDS) and a silicon-drifted XFlash 4030 detector located at the Center for Mineral Technology, Rio de Janeiro, Brazil. The equipment operated at 20 kV, counting time of 60 s, spot size of 5 μm, spectral calibration with a copper standard. Results are presented in the ESM, Supplementary Dataset C with respective structural formulas and calculated end-members.

The U-Pb (LA-ICP-MS and SHRIMP) analyses were performed on two samples at the Geochronological Research Center (CPGeo) of the University of São Paulo. Zircon separation followed standard techniques using methylene iodide and electromagnetic separation with a ferrite hand magnet and a Frantz isodynamic magnetic separator, followed by hand-picking under a stereomicroscope. Selected zircon grains were mounted in 1 cm round epoxy resin mounts, polished using a diamond paste, and cleaned using 10% v/v $HNO_3$ followed by de-ionized water. The mounts were then coated with Au for cathodoluminescence imaging (CL) to reveal internal zoning domains to target isotope analysis.

*In situ* zircon LA-ICP-MS U-Pb analyses were conducted in one sample of the porphyritic facies of the Gentio metagranitoid using a Thermo-Fisher Neptune laser-ablation (LA) multi-collector inductively coupled plasma mass spectrometer (ICP-MS) equipped with one ArF-193 μm Photon laser system (frequency of 6 Hz). Samples were analyzed following standard operating procedures using the methods proposed by Sato et al. (2010). Correction of laser-induced fractionation of $^{206}Pb/^{238}U$ ratio was made with the linear regression method of Kösler et al. (2002). The U-Pb age obtained for the GJ-1 zircon standard was 601±3.5 Ma (Elhlou et al., 2006). Spot size for all analyses was 32 μm. $^{204}Pb$ values were corrected for $^{204}Hg$ interference assuming $^{202}Hg/^{204}Hg$=4.345, the blank and common Pb (Sta-

cey and Kramers, 1975). Zircon U-Pb ages were calculated using the Excel-associated Macro Isoplot (Ludwig, 2003).

Sensitive high-resolution ion microprobe (SHRIMP) age determination was performed in one sample of the equigranular facies using SHRIMP II. The samples were polished together with the TEMORA 2 zircon standard ($^{206}$Pb/$^{238}$U age=416.78±0.33 Ma; Black et al., 2003). The SHRIMP isotopic data were collected in sets of five scans throughout the masses and the TEMORA standard was measured after four unknown analyses. SL13 (238 ppm) was used as a U composition reference (Sato et al., 2014). Analyses with common Pb lower than 10% were used after correction of the measured $^{204}$Pb and assuming the Pb composition of Stacey and Kramers (1975). The data reduction was performed using SQUID 1.06 Excel Macro (Ludwig, 2001), and the statistical assessments were calculated with the ISOPLOT software of Ludwig (2003). The uncertainties in the isotopic ratios and the ages are reported at the 1% level and the weighted mean ages are reported as 95% confidence limits (Sato et al., 2014).

The analyses of whole-rock Sm-Nd isotope were conducted in one sample of the porphyritic and five samples of the equi-granular facies of the Gentio metagranitoid. The Sm and Nd were concentrated using HCl elution and RE and LN cationic exchange columns, following the technical procedures of Petronilho (2009). Laboratory blanks for the chemical procedure yielded maximum values of 40 pg for Nd. The isotopic analyses were acquired in a Triton Thermo Fisher Scientific spectrometer at the CPGeo following the procedure described by Sato et al. (1995). The $^{143}$Nd/$^{144}$Nd average measurements for La Jolla standard is 0.511 857 (46) at 2$\sigma$ level, measured Nd isotopic ratios were normalized to $^{146}$Nd/$^{144}$Nd=0.721 9, and the following constants: $^{143}$Nd/$^{144}$Nd=Nd$_{(CHUR)0}$=0.512 638 and $^{147}$Sm/$^{144}$Nd=0.196 7 (uncertainties at the 2$\sigma$ level). The Sm-Nd $T_{DM}$ model ages were calculated according to DePaolo (1981). The calculated $\varepsilon_{Nd}(t)$ values are referred to as the U-Pb crystallization ages.

## 3 RESULTS
### 3.1 Field Description

The Gentio metagranitoid crops out between Barroso and Dores de Campos cities and it is subdivided in the field into two facies: equigranular and porphyritic spatially closely related.

**Table 2** Major (wt.%), trace elements (ppm) data, and ratios of elements of the Gentio metagranitoid samples

| Detail | Porph | Porph | Porph | Porph | Porph | Porph | Porph | Porph | Porph | Porph | Porph |
|---|---|---|---|---|---|---|---|---|---|---|---|
| Samples | MA-25A | MA-73F | MA-74A2 | MA-74C | MA-89B | MA-89A | MA-90B | MA-91C | MA-73D | MA-113 | MA-90C |
| SiO$_2$ | 71.92 | 70.24 | 74.01 | 74.81 | 65.02 | 70.64 | 71.63 | 68.91 | 66.08 | 69.41 | 73.28 |
| TiO$_2$ | 0.28 | 0.34 | 0.17 | 0.04 | 0.62 | 0.33 | 0.31 | 0.38 | 0.58 | 0.4 | 0.23 |
| Al$_2$O$_3$ | 13.98 | 14.96 | 13.78 | 13.99 | 16.53 | 14.75 | 14.61 | 15.21 | 16.06 | 15.68 | 14.32 |
| FeO$_T$ | 2.3 | 2.56 | 1.27 | 0.87 | 4.21 | 2.8 | 2.41 | 3.24 | 3.87 | 2.52 | 1.7 |
| MnO | 0.04 | 0.03 | 0.02 | 0.02 | 0.06 | 0.05 | 0.04 | 0.06 | 0.06 | 0.06 | 0.03 |
| MgO | 0.72 | 0.79 | 0.36 | 0.07 | 1.74 | 0.91 | 0.72 | 0.99 | 1.67 | 0.72 | 0.48 |
| CaO | 1.64 | 1.94 | 1.22 | 1.44 | 3.92 | 2.03 | 1.94 | 2.38 | 3.77 | 2.04 | 1.71 |
| Na$_2$O | 3.67 | 3.87 | 3.32 | 4.9 | 4.51 | 3.96 | 3.99 | 3.86 | 4.46 | 4.2 | 4.03 |
| K$_2$O | 4.04 | 3.83 | 4.77 | 3.3 | 2.08 | 3.63 | 3.62 | 3.96 | 1.96 | 4 | 3.43 |
| P$_2$O$_5$ | 0.08 | 0.1 | 0.04 | 0 | 0.17 | 0.12 | 0.09 | 0.12 | 0.16 | 0.13 | 0.06 |
| LOI | 1.1 | 1 | 0.7 | 0.4 | 0.8 | 0.5 | 0.4 | 0.6 | 1 | 0.5 | 0.4 |
| Total (-LOI) | 98.7 | 98.7 | 99 | 99.4 | 98.9 | 99.2 | 99.4 | 99.1 | 98.7 | 99.2 | 99.3 |
| Ba | 695 | 1 286 | 1 024 | 663 | 815 | 729 | 768 | 833 | 747 | 1 087 | 902 |
| Rb | 141 | 128 | 157 | 135 | 105 | 138 | 151.1 | 155.3 | 95.2 | 135 | 109 |
| Sr | 191 | 393 | 209 | 188 | 582 | 209 | 219 | 246 | 574 | 372 | 261 |
| Y | 16 | 8 | 8.7 | 24 | 11.7 | 13.4 | 10.5 | 21.6 | 9 | 8.4 | 5.5 |
| Zr | 145 | 195 | 120 | 121 | 159 | 187 | 167 | 179 | 130 | 179 | 123 |
| Nb | 11 | 5.7 | 7.3 | 31 | 9.9 | 9.4 | 11.4 | 14 | 7 | 6.6 | 8.2 |
| Ga | 17.8 | 17.8 | 16.2 | 30 | 20 | 18.2 | 17.3 | 18.9 | 19 | 20.8 | 15.2 |
| Sc | 5 | 4 | 2 | b.d.l | 7 | 6 | 3 | 15 | 7 | 4 | 1 |
| Pb | 10.3 | 10 | 11.1 | b.d.l | 2.6 | 5.4 | 6.2 | 5.7 | 2.7 | 4.8 | 5.8 |
| Zn | 38 | 47 | 22 | 43 | 75 | 52 | 46 | 55 | 70 | 48 | 28 |
| Ta | 1.1 | 1 | 1.7 | b.d.l. | 1.1 | 1.2 | 0.7 | 1.4 | 1.5 | 1.1 | 1.1 |
| Th | 17.4 | 23 | 16.5 | b.d.l | 9.7 | 18.8 | 15.4 | 25 | 6.7 | 14.6 | 9.2 |
| U | 2 | 1.8 | 1.8 | b.d.l | 1.7 | 1.4 | 1.4 | 1.6 | 1.8 | 1.2 | 0.8 |
| Hf | 4.8 | 4.3 | 4.1 | b.d.l | 3.5 | 5.6 | 4.7 | 5.6 | 2.5 | 4.5 | 3.5 |
| Rb/Sr | 0.7 | 0.3 | 0.8 | 0.7 | 0.2 | 0.7 | 0.7 | 0.6 | 0.2 | 0.4 | 0.4 |
| Sr/Ba | 0.3 | 0.3 | 0.2 | 0.3 | 0.7 | 0.3 | 0.3 | 0.3 | 0.8 | 0.3 | 0.3 |

**Table 2** Continued

| Detail | Equi | Equi | Equi | Equi | Equi | Equi | Equi | Equi | Equi | Equi |
|---|---|---|---|---|---|---|---|---|---|---|
| Samples | MA-24A | MA-25C | MA-73C | MA-73D1 | MA-74B | MA-89E | MA-91A | MA-101 | MA-89G | NAT-38 |
| $SiO_2$ | 68.75 | 71.01 | 68.58 | 64.74 | 70.26 | 64.7 | 71.82 | 69.15 | 73.96 | 70.81 |
| $TiO_2$ | 0.36 | 0.21 | 0.41 | 0.65 | 0.24 | 0.67 | 0.32 | 0.43 | 0.09 | 0.36 |
| $Al_2O_3$ | 15.35 | 15.29 | 15.81 | 16.65 | 15.63 | 16.61 | 14.31 | 15.33 | 14.33 | 14.64 |
| $FeO_T$ | 2.69 | 1.49 | 2.83 | 4.27 | 1.79 | 4.47 | 1.97 | 2.6 | 0.72 | 2.3 |
| MnO | 0.07 | 0.03 | 0.04 | 0.06 | 0.03 | 0.06 | 0.03 | 0.04 | 0.01 | 0 |
| MgO | 0.85 | 0.34 | 1 | 1.79 | 0.61 | 1.79 | 0.39 | 0.88 | 0.19 | 0.63 |
| CaO | 1.5 | 1.96 | 2.71 | 4.03 | 1.89 | 4.24 | 1.47 | 2.14 | 1.07 | 2.08 |
| $Na_2O$ | 3.97 | 4.6 | 4.19 | 4.58 | 4.09 | 4.43 | 3.62 | 4.09 | 3.4 | 4.05 |
| $K_2O$ | 5.02 | 3.71 | 2.99 | 2.1 | 3.84 | 1.89 | 4.73 | 3.86 | 5.28 | 3.05 |
| $P_2O_5$ | 0.11 | 0.07 | 0.15 | 0.17 | 0.09 | 0.19 | 0.09 | 0.16 | 0.05 | 0.1 |
| LOI | 1 | 1.1 | 0.8 | 0.6 | 1.1 | 0.6 | 0.9 | 0.9 | 0.5 | 0.8 |
| Total (-LOI) | 98.7 | 98.7 | 98.7 | 99 | 98.5 | 99.1 | 98.8 | 98.7 | 99.1 | 98 |
| Ba | 1 381 | 791 | 1 911 | 834 | 1 758 | 666 | 1 155 | 1 493 | 1 814 | 1 414 |
| Rb | 170 | 117 | 93.8 | 102 | 161 | 99 | 148 | 150 | 104 | 91.1 |
| Sr | 241 | 239 | 528 | 604 | 365 | 676 | 217 | 355 | 309 | 365 |
| Y | 17.7 | 9.1 | 7.6 | 11.5 | 6.8 | 17.1 | 8.2 | 8 | 3.8 | 5.6 |
| Zr | 195 | 124 | 273 | 193 | 110 | 229 | 205 | 275 | 92 | 215 |
| Nb | 13 | 7.7 | 6.4 | 9.7 | 6.9 | 11.7 | 11.1 | 6.8 | 4.6 | 9.3 |
| Ga | 18.9 | 19.3 | 17.6 | 19.9 | 16.7 | 21.3 | 19.6 | 21.9 | 15.7 | 18.4 |
| Sc | 7 | 2 | 5 | 8 | 3 | 8 | 3 | 3 | 2 | 14 |
| Pb | 15.7 | 9.4 | 8.4 | 2.3 | 8.5 | 2.1 | 10.3 | 8.4 | 5.9 | 17.8 |
| Zn | 53 | 27 | 52 | 72 | 33 | 75 | 47 | 64 | 8 | 46.8 |
| Ta | 1.7 | 1.5 | 1.2 | 0.9 | 1.5 | 1.9 | 1.9 | 1 | 1.2 | b.d.l. |
| Th | 17.2 | 20.8 | 43.9 | 9.6 | 15.8 | 12.1 | 23.9 | 26.2 | 20.9 | 18.1 |
| U | 2.4 | 5 | 3.3 | 1.3 | 2.1 | 1.4 | 2.3 | 2.8 | 2.2 | 1.9 |
| Hf | 5.2 | 3.9 | 7.6 | 5.1 | 2.7 | 5.9 | 4.9 | 6.7 | 2.8 | 5.2 |
| Rb/Sr | 0.7 | 0.5 | 0.2 | 0.2 | 0.4 | 0.1 | 0.7 | 0.4 | 0.3 | 0.4 |
| Sr/Ba | 0.2 | 0.3 | 0.3 | 0.7 | 0.2 | 1 | 0.2 | 0.2 | 0.2 | 0.3 |

b.d.l. Below detection limit; Porph. porphyritic facies; Equi. equigranular facies.

**Table 3** Rare earth elements data (ppm) and ratio of the Gentio metagranitoid samples

| Samples | La | Ce | Pr | Nd | Sm | Eu | Gd | Tb | Dy | Ho | Er | Tm | Yb | Lu | Eu/Eu* |
|---|---|---|---|---|---|---|---|---|---|---|---|---|---|---|---|
| MA-25A | 36.5 | 67.5 | 6.96 | 22.8 | 4.25 | 0.64 | 3.64 | 0.6 | 3.07 | 0.69 | 1.60 | 0.22 | 1.27 | 0.19 | 0.5 |
| MA-73F | 51.6 | 131.4 | 9.59 | 29.5 | 4.22 | 0.83 | 2.72 | 0.35 | 1.42 | 0.26 | 0.73 | 0.13 | 0.61 | 0.17 | 0.8 |
| MA-74A2 | 27.1 | 60 | 5.33 | 18 | 3 | 0.62 | 2.20 | 0.33 | 1.72 | 0.3 | 0.88 | 0.14 | 0.74 | 0.13 | 0.7 |
| MA-89B | 45.9 | 97.5 | 8.45 | 30.8 | 4.65 | 1.19 | 3.43 | 0.47 | 2.08 | 0.45 | 1.27 | 0.17 | 0.94 | 0.15 | 0.9 |
| MA-89A | 33.8 | 72.1 | 6.24 | 21.3 | 3.84 | 0.67 | 3.5 | 0.51 | 2.41 | 0.48 | 1.29 | 0.19 | 1.04 | 0.19 | 0.6 |
| MA-90B | 40.2 | 70.7 | 6.92 | 20.8 | 3.78 | 0.74 | 2.73 | 0.39 | 1.95 | 0.32 | 1.06 | 0.15 | 0.80 | 0.12 | 0.7 |
| MA-91C | 84.0 | 131 | 14.62 | 50.2 | 7.57 | 0.85 | 6.43 | 0.86 | 3.92 | 0.76 | 2.1 | 0.31 | 1.60 | 0.22 | 0.4 |
| MA-73D | 38.9 | 107.7 | 7.68 | 22.3 | 3.76 | 1.13 | 3.19 | 0.38 | 1.56 | 0.35 | 0.99 | 0.14 | 0.84 | 0.11 | 1 |
| MA-113 | 46.9 | 89.1 | 8.07 | 26.3 | 4.00 | 0.87 | 2.79 | 0.39 | 1.90 | 0.32 | 0.8 | 0.1 | 0.72 | 0.1 | 0.8 |
| MA-90C | 21.6 | 46 | 3.95 | 14.7 | 2.11 | 0.62 | 1.54 | 0.16 | 0.77 | 0.19 | 0.37 | 0.09 | 0.53 | 0.07 | 1.1 |
| MA-24A | 24.8 | 47.2 | 5.19 | 16.7 | 3.3 | 0.63 | 3.42 | 0.59 | 3.69 | 0.72 | 1.94 | 0.27 | 1.53 | 0.24 | 0.6 |
| MA-25C | 42.9 | 77.3 | 8.05 | 26.1 | 4.15 | 0.71 | 2.38 | 0.32 | 1.57 | 0.3 | 0.92 | 0.12 | 0.61 | 0.1 | 0.7 |
| MA-73C | 73.1 | 152.3 | 10.82 | 35.8 | 4.76 | 0.87 | 2.89 | 0.33 | 1.32 | 0.26 | 0.75 | 0.10 | 0.52 | 0.13 | 0.7 |
| MA-73D1 | 44.0 | 98 | 8.49 | 28.7 | 4.69 | 1.19 | 3.25 | 0.46 | 2.32 | 0.44 | 1.22 | 0.16 | 0.96 | 0.13 | 0.9 |
| MA-74B | 34.1 | 51.5 | 4.76 | 14.6 | 2.42 | 0.62 | 1.49 | 0.24 | 1.36 | 0.2 | 0.78 | 0.11 | 0.71 | 0.06 | 1.0 |
| MA-89E | 48.5 | 90.3 | 9.27 | 32.4 | 5.03 | 1.29 | 4.01 | 0.56 | 3.3 | 0.6 | 1.78 | 0.3 | 1.71 | 0.31 | 0.9 |
| MA-91A | 58 | 95.5 | 9.72 | 31.3 | 4.24 | 0.75 | 2.67 | 0.35 | 1.93 | 0.28 | 0.8 | 0.12 | 0.63 | 0.09 | 0.7 |
| MA-101 | 102.4 | 134.8 | 14.20 | 44 | 5.11 | 0.97 | 2.68 | 0.34 | 1.57 | 0.24 | 0.66 | 0.13 | 0.66 | 0.12 | 0.8 |
| MA-89G | 27 | 49.5 | 4.30 | 13.5 | 2.27 | 0.58 | 1.51 | 0.18 | 0.96 | 0.16 | 0.36 | 0.07 | 0.35 | 0.05 | 1 |
| NAT-38 | 32.9 | 56.83 | 5.57 | 18.15 | 2.63 | 0.85 | 2.06 | 0.22 | 1.11 | 0.19 | 0.5 | 0.07 | 0.44 | 0.07 | 1.1 |

The Gentio metagranitoid has about 104 km² of the mapped area as its western limit is not yet defined. This body is NE-SW oriented and increases in area on the map from east to west (Fig. 1). In outcrop scale, both facies are almost always associated with the rocks of the equigranular facies crosscutting the porphyritic one. Their contacts are sharp, angular, and/or sinuous. The different equigranular intrusions are easily individualized by their color index and texture (Fig. 2a) and usually exhibit tabular (dyke-like) and/or sinuous to a rounded shape.

This metagranitoid is also cut by pegmatites and hololeucocratic felsic dykes and hosts xenoliths of metamafic (Fig. 2b) and metaultramafic rocks of the Dores de Campos metavolcanic-sedimentary sequence and more rarely of a biotite orthogneiss. Additionally, dikes associated with equigranular facies of the Gentio metagranitoid crosscuts amphibolites and metaultramafic

rocks of the Dores de Campos metavolcanic-sedimentary sequence.

The porphyritic facies are characterized by the presence of 15% to 20% of euhedral to subhedral feldspar phenocrysts (plagioclase and K-feldspar) varying from 1.5 to 8 cm, with a typical size of 2 cm. The phenocrysts are immersed in a medium-grained equigranular matrix of plagioclase, K-feldspar, quartz, and biotite. In the field, the feldspar phenocrysts are either oriented (Fig. 2c) or randomly arranged (Fig. 2d). The most prominent primary structure observed in the Gentio metagranitoid is the magmatic foliation marked by the orientation of the feldspar phenocrysts, which shows ENE-WSW direction and mostly dipping moderately to steeply (or sub vertically) to NNW or SSE (Fig. 3a). This trend is subparallel to the main tectonic foliation described in the host rocks, with E-W to ENE-WSW direction and
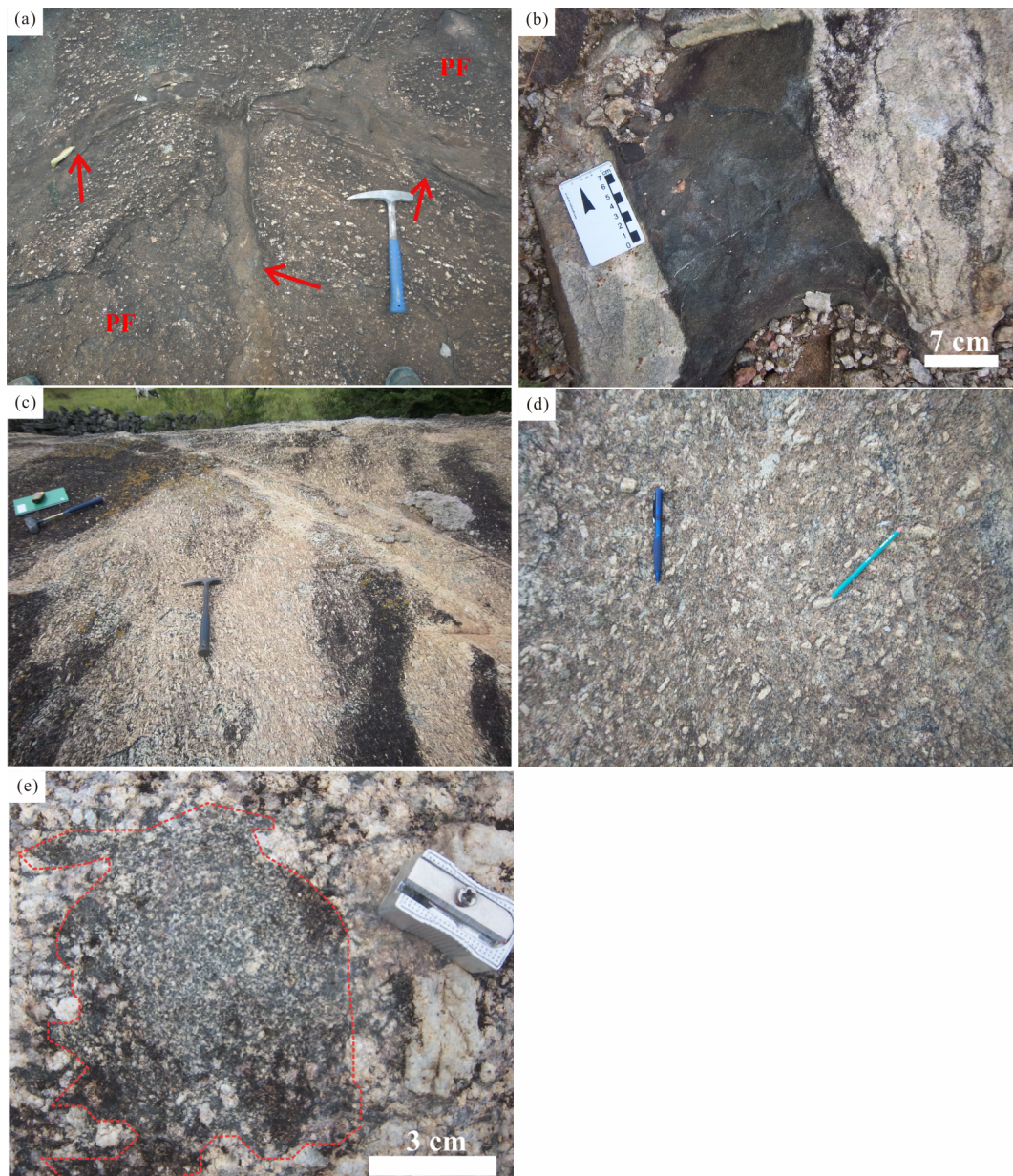


**Figure 2.** Field photographs showing (a) the relationships of different magmatic pulses observed in the Gentio metagranitoid; red arrows. equigranular facies; PF. porphyritic facies; (b) xenolith of amphibolite with angular and sharp contact, with the formation of biotite in the contact with porphyritic facies; (c) the porphyritic texture of the Gentio metagranitoid with the magmatic orientation of tabular phenocrysts of feldspar; and (d) chaotic arrangement; (e) mafic enclave partially dissolved in the porphyritic facies.
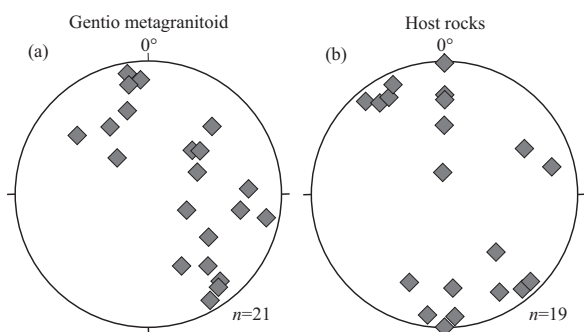
**Figure 3.** Equal area projection (lower hemisphere) stereo plots showing poles of the magmatic foliation of the Gentio metagranite (a) and of the tectonic foliation of the host rocks (b). See the text for details.

dipping moderately to steeply to NNW or SSE (Fig. 3b). The tectonic foliation of the host rocks was developed under amphibolite facies metamorphic conditions, before the emplacement of the metagranitoid. Both magmatic and tectonic foliations also present a small population of measurements dipping moderately to NE. Other observed structures in the studied body include syn-magmatic shear bands with different orientations and low-temperature post-magmatic shear bands related to a younger metamorphic episode at greenschist-facies condition.

The xenolith of metamafic (Fig. 2b), metaultramafic, and rarely gneissic rocks have variable sizes and angular, tabular, and rounded shapes. Mafic enclaves (up to 10 cm in size) were also observed (Fig. 2e).

### 3.2 Petrography

The Gentio metagranitoid varies from hololeucrocratic to leucocratic and its mineral assemblage is represented by plagioclase (25% to 50%), microcline+orthoclase (3% to 35%), quartz (23% to 35%), and biotite (2% to 18%). Its modal composition lies within the ranges of monzogranite, granodiorite, and a lesser amount of tonalite. The porphyritic facies matrix has similar mineralogy to the equigranular facies (Figs. 4a and 4b) and contains 15%–20% of plagioclase and K-feldspar phenocrysts.

The accessory phases in both facies are represented by titanite, zircon, allanite, apatite, and opaque minerals while epidote, clinozoisite, zoisite, chlorite, muscovite, and sericite re-

place primary minerals.

Plagioclase often has an albitic rim, can present inclusions of apatite, zircon, and allanite, and be partially replaced by sericite, clinozoisite, zoisite, and epidote (Fig. 4). K-feldspar consists of subhedral to euhedral perthitic crystals and sometimes host inclusions of plagioclase and quartz. Quartz grains were recrystallized and show rare inclusions of zircon and titanite.

Biotite occurs as individual crystals or as clusters of small tabular grains, may host inclusions of apatite, zircon, and rarely needle-like rutile. It can be completely or partially replaced by muscovite, titanite, chlorite, zoisite, and epidote. Primary titanite is observed as individual grains with euhedral shape while metamorphic titanite is anhedral and occurs as an individual or clustered grains replacing biotite and associated with epidote.

At the microscopic scale, the magmatic features are represented by euhedral crystals of apatite, titanite, and zircon with the latter showing oscillatory zoning. Metamorphic and deformational features are also represented by myrmekitic intergrowth; kink bands in biotite; quartz blebs in biotite; and albitization of plagioclase.

The mineral assemblage of the amphibolite xenoliths from the Dores de Campos metavolcanic-sedimentary sequence comprises amphibole, plagioclase, and quartz (less than 3%). Amphibole grains are partially replaced by biotite and/or epidote.

### 3.3 Mineral Chemistry

Biotite is the most abundant mafic mineral and it can reach up to 18%. It shows a homogeneous chemical composition and displays a Fe/(Fe+Mg) ratio from 0.47 to 0.56, while total $Al^{IV}$ content varies from 2.94 to 3.15 apfu (ESM, Supplementary Dataset A). Also, biotite exhibits low Ti content (0.16–0.22 apfu) and its composition is close to annite. In the ternary diagrams of Nockolds (1947) and Abdel-Rahman (1994), the biotite composition falls within the field of the only mafic mineral (Fig. 5a), and in the calc-alkaline orogenic suites (Fig. 5b).

Plagioclase is characterized by a more calcic core with a more albitic rim (Figs. 5c and 5d), their composition varies from andesine to albite (ESM, Supplementary Dataset B and C). The composition of the plagioclase from equigranular facies overlaps with the porphyritic facies and there is no compositional difference between plagioclase from the matrix and
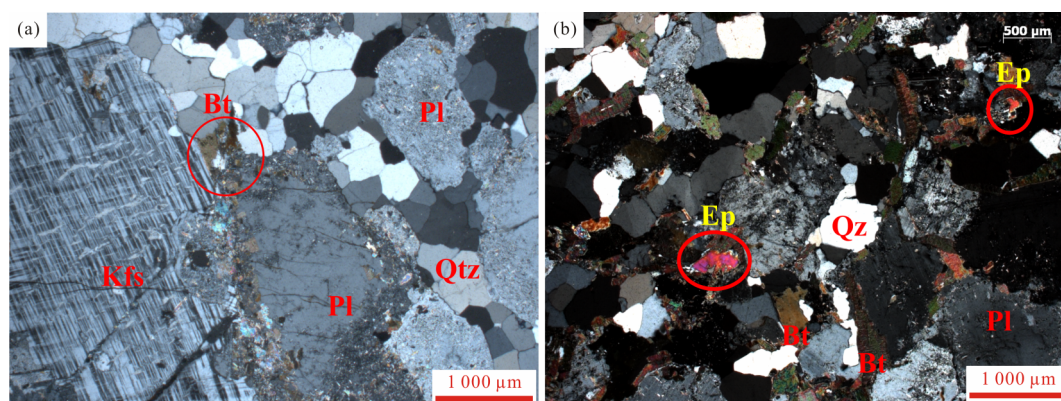


**Figure 4.** Photomicrographs showing the different textures of the Gentio metagranitoid. (a) Porphyritic facies with phenocryst of alkali-feldspar (Kfs); (b) equigranular facies with tonalite modal composition bearing quartz (Qtz), biotite (Bt), plagioclase (Pl), and epidote (Ep).
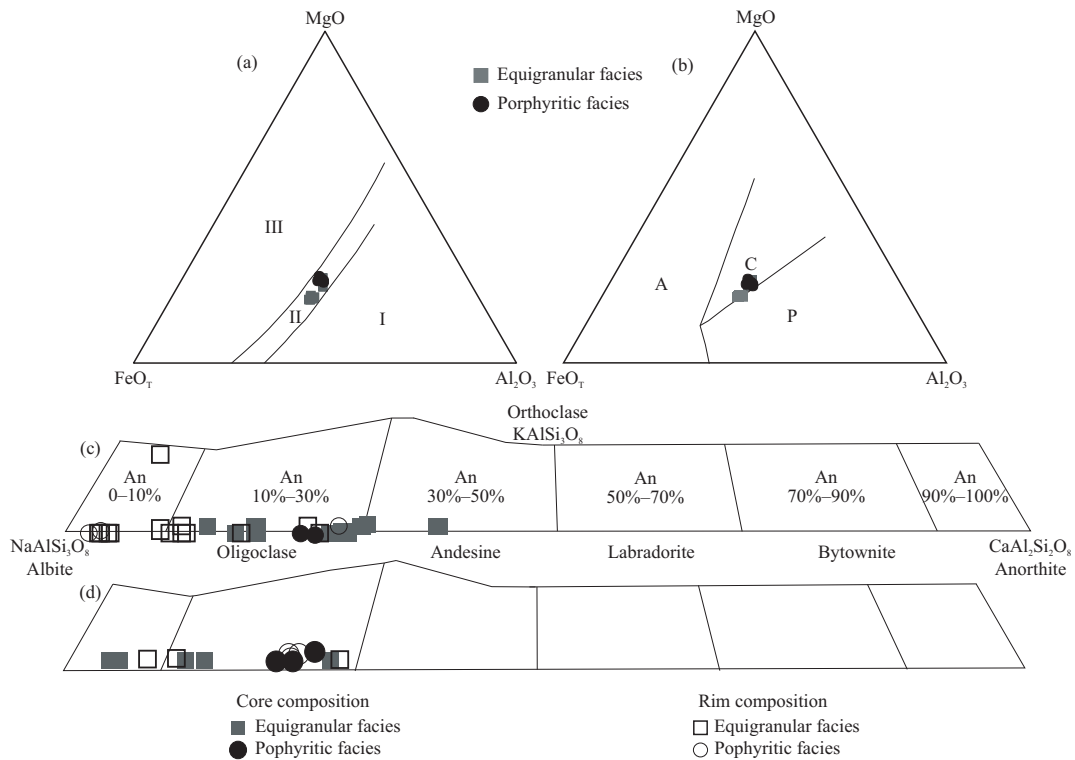
**Figure 5.** Ternary diagrams MgO-FeO$_T$-Al$_2$O$_3$ applied to the composition of biotite and feldspar classification diagram from Gentio metagranitoid. (a) I. Biotite associated with muscovite; II. biotite as the only mafic mineral; and III. biotite associated with hornblende, pyroxene, or olivine (Nockolds, 1947); (b) A. biotite from anorogenic alkaline suites; P. biotite in peraluminous suites (including S-type); and C. biotite in calc-alkaline orogenic suites (Abdel-Rahman, 1994); (c) analyses of plagioclase by SEM-EDS; (d) analyses of plagioclase by microprobe.

phenocrysts (Figs. 5c and 5d). The Sr content is relatively homogenous (0.04–0.07 apfu) in all samples.

### 3.4 Whole-Rock Chemistry

Based on its geochemistry, Gentio metagranitoid samples can be separated into two main groups (Fig. 6 and Table 2): SiO$_2$ content varying from 65 wt.% to 67 wt.% (low-SiO$_2$ group); SiO$_2$ from 69 wt.% to 75 wt.% (high-SiO$_2$ group).

The low-SiO$_2$ group includes two samples from the equigranular facies and two from the porphyritic facies (Fig. 6) and presents chemical composition compatible with granodiorite (Middlemost, 1985, diagram is not presented here). The high-SiO$_2$ group includes the other seventeen samples and their chemistry is compatible with granite (Middlemost, 1985). According to the classification proposed by Frost et al. (2001, diagram is not presented here), both groups are classified as magnesian with FeO$_T$/(FeO$_T$+MgO) values between 0.7 and 0.8, except one sample (MA-74C, porphyritic facies) that presents value of 0.9. The CIPW normative orthoclase+albite+quartz content for the low SiO$_2$ group varies between 70% and 72% while for the high-SiO$_2$ group ranges from 81% to 92%.

In the Harker diagram, the studied samples exhibit a scattered distribution. Samples with similar MgO, K$_2$O, Na$_2$O, CaO, FeO$_T$ contents can vary greatly concerning SiO$_2$ (Fig. 6). If the whole group of the sample is considered, no coherent change with increasing SiO$_2$ content is observed.

The low-SiO$_2$ group always plots separately from the rest and exhibits higher contends for all oxides except for K$_2$O (Fig. 6). This group plots in the field of the calc-alkaline series,

while the samples of the high-SiO$_2$ group fall in the high-K calc-alkaline series (Fig. 7a). In the B-A diagram modified by Villaseca et al. (1998), the low-SiO$_2$ group plots in the metaluminous field, while the majority of samples from the high-SiO$_2$ group plot in the low peraluminous field (Fig. 7b).

Chondrite-normalized REE patterns exhibit some constant characteristics (Figs. 8a and 8b), and enrichment of LREE in comparison to HREE and variable Eu anomalies (Table 3). The low-SiO$_2$ samples of the equigranular facies are more enriched in the heavy rare earth elements than most of the high-SiO$_2$ samples (Fig. 8b).

Spider diagrams normalized to the average continental crust (Weaver and Tarney, 1984) display a fairly horizontal pattern (Figs. 8c and 8d). No coherent variation with increasing SiO$_2$ is observed and the low-SiO$_2$ samples of the equigranular facies are less enriched in the most incompatible elements than the high-SiO$_2$ samples (Figs. 8c and 8d). Ba (367 ppm–1 911 ppm), Rb (91 ppm–195 ppm), and Th (7 ppm–44 ppm) display mean abundances higher than the normalizing parameter average crust while Sr (69 ppm–676 ppm), Zr (71 ppm–275 ppm), and Nb (5 ppm–31 ppm) are slightly lower than it.

### 3.5 Zircon Saturation Temperatures

The Zr saturation temperature method ($T_{Zr}$) applies to most intermediate to felsic metaluminous-peraluminous magmas that present a major element concentration [$M$=(Na+K+2Ca)/(Al×Si)] between 0.9 and 1.7 (Watson and Harrison, 1983). Our samples present $M$ values between 1.1 and 1.5 and for the $T_{Zr}$ calculation we have used the revised equations from Boehnke et al. (2013).
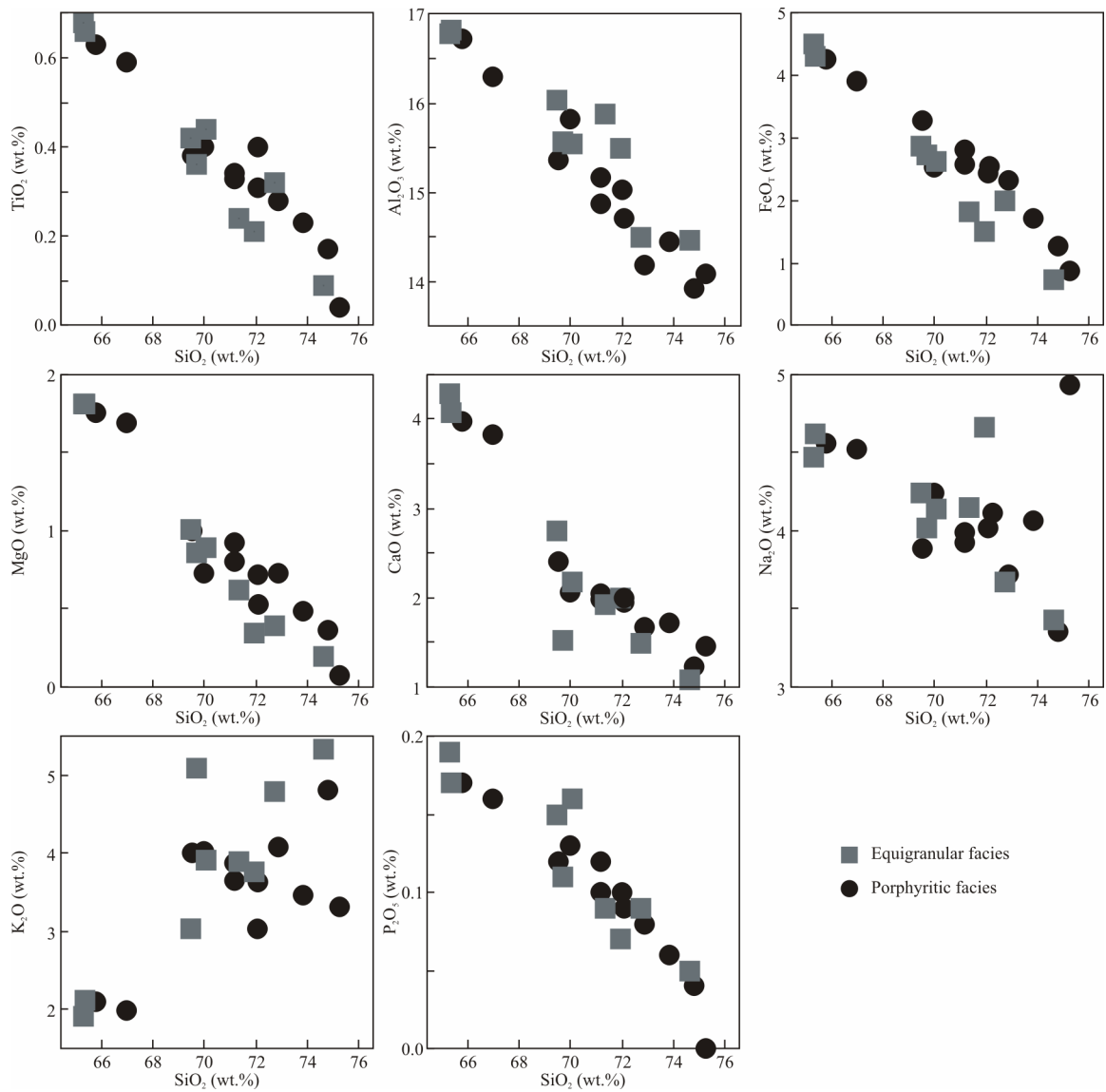
**Figure 6.** Harker variation diagrams for major elements from the Gentio metagranitoid samples.
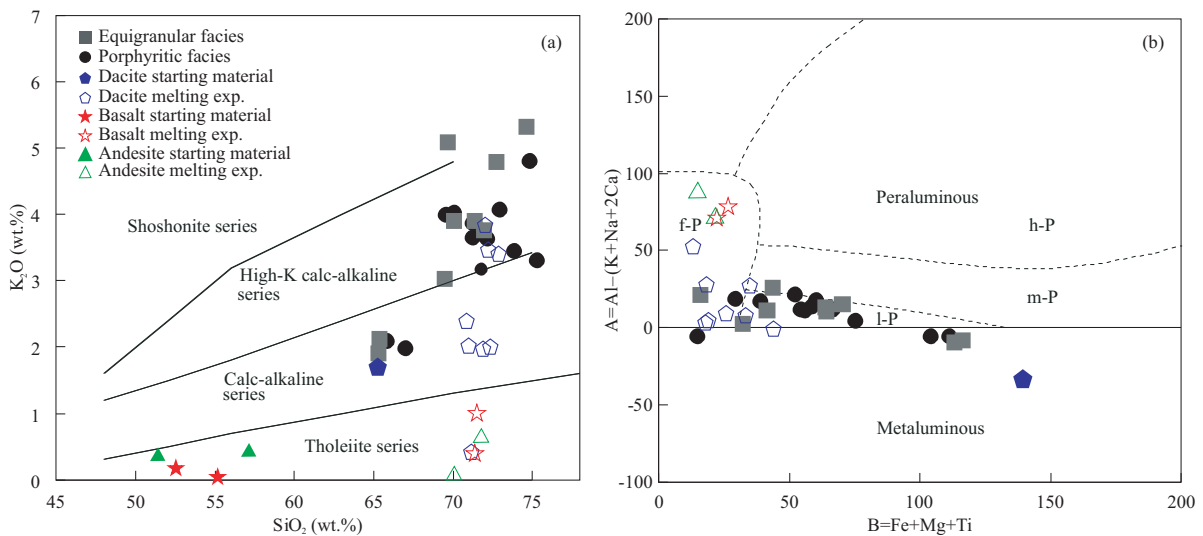


**Figure 7.** Discriminant diagrams for the Gentio metagranitoid samples and experimental data. (a) SiO$_2$ vs. K$_2$O (Peccerillo and Taylor, 1976); and (b) Al–(K+Na+2C) vs. Fe+Mg+Ti (Villaseca et al., 1998); h-P. highly peraluminous granitoids; m-P. moderately peraluminous granitoids; l-P. low peraluminous granitoids; f-P. highly felsic peraluminous granitoids. Dacite data from Conrad et al. (1988); basalt and andesite data from Beard and Lofgren (1991). See text for details.
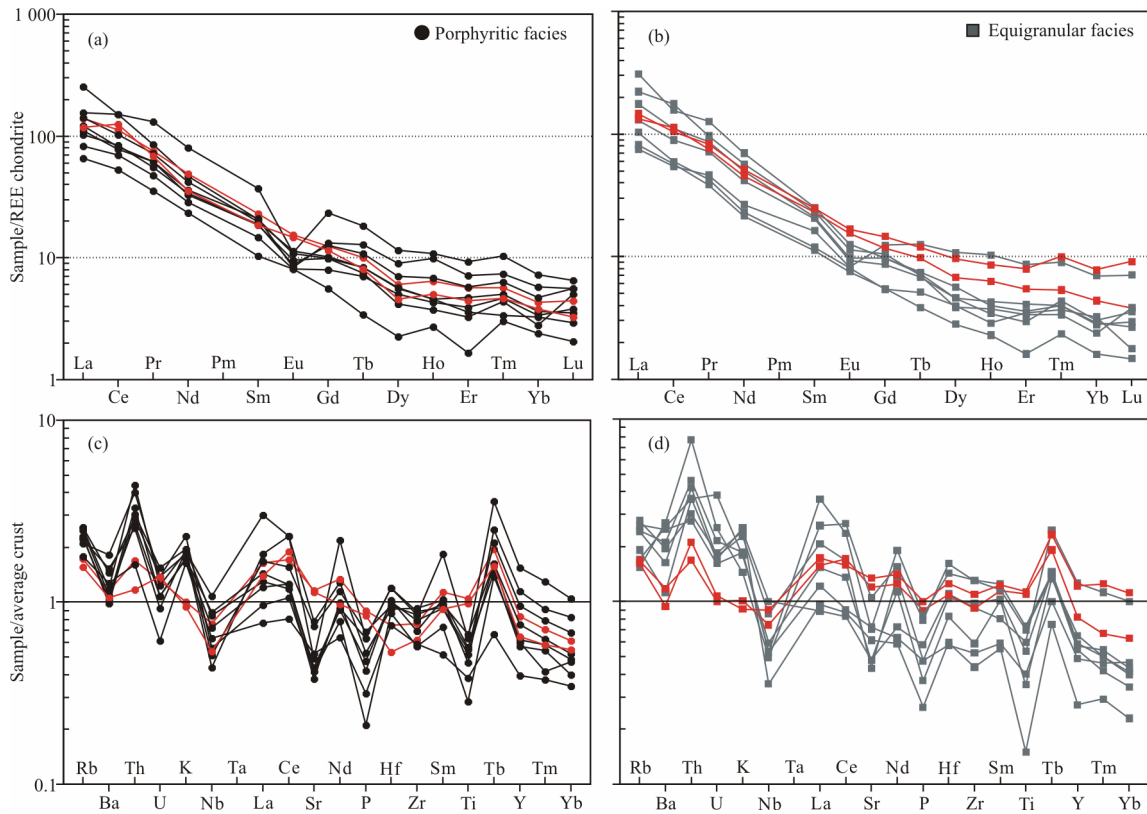
**Figure 8.** Chondrite normalized rare earth elements diagram (Nakamura, 1974) and average crust normalized spider diagrams (Weaver and Tarney, 1984) for porphyritic (a) and (c) and equigranular (b) and (d) facies from Gentio metagranitoid. The samples in red are the low-$SiO_2$ group.

**Table 4**   Calculated zircon saturation temperature of the Gentio metagranitoid (Boehnke et al., 2013)

| Samples | A/CNK | $M$ | $D$ (Zr) | $T$ (°C) | Samples | A/CNK | $M$ | $D$ (Zr) | $T$ (°C) |
|---------|-------|-----|----------|----------|---------|-------|-----|----------|----------|
| MA-25A | 1.04 | 1.22 | 3 429.8 | 751 | MA-24A | 1.04 | 1.26 | 2 549.5 | 777 |
| MA-73F | 1.07 | 1.22 | 2 554.7 | 782 | MA-25C | 1.01 | 1.27 | 4 029.6 | 728 |
| MA-74A2 | 1.07 | 1.15 | 4 154.1 | 739 | MA-73C | 1.05 | 1.26 | 1 823.6 | 814 |
| MA-74C | 0.98 | 1.26 | 4 112.9 | 728 | MA-73D1 | 0.97 | 1.45 | 2 585.2 | 752 |
| MA-89B | 0.98 | 1.43 | 3 122.1 | 735 | MA-74B | 1.09 | 1.18 | 4 536.5 | 727 |
| MA-89A | 1.04 | 1.24 | 2 665.6 | 774 | MA-89E | 0.97 | 1.45 | 2 171.3 | 770 |
| MA-90B | 1.04 | 1.23 | 2 981.8 | 764 | MA-91A | 1.04 | 1.22 | 2 428.8 | 788 |
| MA-91C | 1.02 | 1.30 | 2 784.9 | 762 | MA-101 | 1.04 | 1.27 | 1 811.0 | 815 |
| MA-73D | 0.98 | 1.41 | 3 834.0 | 718 | MA-89G | 1.08 | 1.14 | 5 427.0 | 714 |
| MA-113 | 1.05 | 1.25 | 2 774.0 | 769 | NAT-38 | 1.07 | 1.20 | 2 317.4 | 795 |
| MA-90C | 1.06 | 1.18 | 4 042.7 | 738 | | | | | |

In Table 4, we present calculated zircon saturation temperatures for the Gentio metagranitoid, and the results show that the low-$SiO_2$ group presents $T_{Zr}$ of 718–770 °C and the high-$SiO_2$ group exhibits values between 714 and 788 °C. However, two samples of the high-$SiO_2$ group yielded $T_{Zr}$ of 814–815 °C.

### 3.6   Geochronology

Zircon grains from the porphyritic facies were dated by the LA-ICP-MS and are pink, prismatic, pyramidal, or bipyramidal and present length/ratios of 1 : 2 to 1 : 4. Cathodoluminescence images show homogeneous patchy to oscillatory magmatic growth patterns (Fig. 9a). Some grains have inherited nuclei and metamorphic rims. Analyzes of twelve grains cluster defined a concordia crystallization age of 2 119±10 Ma (MSWD=2.1) (Table 6, Fig. 9b). Analyses of inherited zircon grains yielded nearly concordant [207]Pb/[206]Pb ages of 2 213±36 and 2 438±20 Ma while three zircon grains exhibited homogeneous dark colors yielding metamorphic concordia age of 659±43 Ma (Table 6).

Zircon grains from the equigranular facies were dated by the SHRIMP and varied from 125 to 320 μm in size (Fig. 9c). They are subhedral or prismatic and sub-rounded terminations are common. Zircon grains are translucent to opaque and range from brown to dark brown in color. In the CL image, the crystals

**Table 5** Summary of the SHRIMP U-Pb zircon analytical data, Gentio's equigranular facies

| Spot | U (ppm) | Th/U | % common Pb | 207Pb/206Pb | % error | 207Pb/235U | % error | 206Pb/238U | % error | Error cor. | 207Pb/206Pb age (Ma) | % error | 206Pb/238U age (Ma) | % error | % DISC | Error cor. |
|---|---|---|---|---|---|---|---|---|---|---|---|---|---|---|---|---|
| NAT38-1.1 | 363 | 0.38 | 0.52 | 0.124 | 0.6 | 3.92 | 2.4 | 0.2367 | 2.2 | 0.91 | 1 957 | 18 | 1 369 | 27 | 43 | 0.91 |
| NAT38-2.1 | 536 | 0.92 | 1.22 | 0.105 | 0.8 | 1.84 | 3.1 | 0.1402 | 2.3 | 0.738 | 1 530 | 39 | 846 | 18 | 81 | 0.738 |
| NAT38-3.1 | 407 | 0.79 | 1.12 | 0.121 | 0.8 | 3.18 | 2.8 | 0.2055 | 2.2 | 0.783 | 1 837 | 31 | 1 205 | 24 | 53 | 0.783 |
| NAT38-4.1 | 383 | 0.41 | 0.14 | 0.128 | 0.5 | 6.13 | 2.3 | 0.3513 | 2.2 | 0.964 | 2 051 | 11 | 1 941 | 37 | 6 | 0.964 |
| NAT38-5.1 | 281 | 0.6 | 0.08 | 0.129 | 0.4 | 5.96 | 2.2 | 0.3371 | 2.2 | 0.975 | 2 074 | 9 | 1 873 | 36 | 11 | 0.975 |
| NAT38-6.1 | 270 | 0.86 | 0.13 | 0.126 | 0.5 | 5.01 | 2.3 | 0.2902 | 2.3 | 0.971 | 2 033 | 10 | 1 643 | 33 | 24 | 0.971 |
| NAT38-7.1 | 408 | 0.28 | 0.12 | 0.123 | 0.5 | 4.67 | 2.2 | 0.2767 | 2.2 | 0.97 | 1 990 | 10 | 1 575 | 30 | 26 | 0.97 |
| NAT38-8.1 | 406 | 1.01 | 0.13 | 0.125 | 0.5 | 4.9 | 2.3 | 0.2877 | 2.2 | 0.965 | 2 010 | 10 | 1 630 | 31 | 23 | 0.965 |
| NAT38-9.1 | 662 | 0.32 | 0.56 | 0.1 | 0.6 | 1.9 | 2.4 | 0.1446 | 2.2 | 0.896 | 1 532 | 20 | 870 | 18 | 76 | 0.896 |
| NAT38-10.1 | 509 | 0.5 | 1.37 | 0.121 | 0.4 | 3.04 | 2.8 | 0.2000 | 2.2 | 0.772 | 1 802 | 32 | 1 175 | 23 | 53 | 0.772 |
| NAT38-11.1 | 400 | 0.63 | 0.06 | 0.126 | 0.5 | 5.17 | 2.3 | 0.2994 | 2.2 | 0.977 | 2 032 | 9 | 1 688 | 33 | 20 | 0.977 |
| NAT38-12.1 | 529 | 0.81 | 0.36 | 0.123 | 0.4 | 4.11 | 2.3 | 0.2476 | 2.2 | 0.951 | 1 960 | 13 | 1 426 | 28 | 37 | 0.951 |
| NAT38-13.1 | 473 | 0.12 | 0.75 | 0.123 | 0.4 | 3.86 | 2.5 | 0.2390 | 2.2 | 0.884 | 1 915 | 21 | 1 381 | 27 | 39 | 0.884 |
| NAT38-14.1 | 398 | 0.77 | 0.47 | 0.127 | 0.4 | 4.79 | 2.3 | 0.2821 | 2.2 | 0.944 | 2 001 | 14 | 1 602 | 31 | 25 | 0.944 |
| NAT38-15.1 | 383 | 0.58 | 1.17 | 0.115 | 1.4 | 2.56 | 3.5 | 0.1766 | 2.3 | 0.638 | 1 718 | 50 | 1 048 | 22 | 64 | 0.638 |

display metamitic features, unzoned portions, and small edges of metamorphic overgrowths that were not dated. Fifteen SHRIMP data (Table 5) show Th/U values varying from 0.12 to 1. The upper intercept age is 2 111±15 Ma (MSWD=1.0), whereas the lower intercept is 530±32 Ma (Fig. 9d).

### 3.7 Sm/Nd Isotopes

The Sm-Nd analytical data are presented in Table 7, where isotopic parameters were calculated for the U-Pb crystallization ages of 2 120 and 2 111 Ma, respectively. The Gentio metagranitoid presents $^{147}Sm/^{144}Nd$ ratios between 0.081 and 0.120, and the Sm/Nd $T_{DM}$ model ages can be separated into two groups: Archean (2.87–2.51 Ga) with $\varepsilon_{Nd}(2.1)$ values ranging from -2.6 to -5.4 and a Paleoproterozoic (2.48–2.36 Ga) with $\varepsilon_{Nd}(2.1)$ varying between -0.7 and -2.4. Of the six samples analyzed, only one belongs to the low-SiO$_2$ group (MA-73D1, Table 7) which presents the $T_{DM}$ model age of 2.46 Ga and $\varepsilon_{Nd}(2.1)$ of -2.

In the $\varepsilon_{Nd}(0)$ vs. crystallization age diagram (Fig. 10) most samples overlap with the field that represents the isotopic evolution of the Paleoproterozoic continental crust of the São Francisco Craton.

## 4 DISCUSSION

### 4.1 Zircon Saturation Temperature

$T_{Zr}$ model gives the temperature at which zircon saturation (and precipitation) in the melt has occurred, which could be reached at any time and temperature during the crystallization history of the magma. If the magma is saturated in Zr at the source, zircon will precipitate early and the calculated $T_{Zr}$ will provide a maxima estimate crystallization temperature of the magma. On the other hand, if the magma is undersaturated in zircon at the source, zircon will be in a later phase and $T_{Zr}$ will provide a minimum estimate of magma crystallization temperature.

Experimental studies have demonstrated that the solubility of Zr during anatexis is mainly a function of temperature, the composition of the melt, and Zr content of the source (Boehnke et al., 2013; Watson and Harrison, 1983). The parameter $M$ [$=(Na+K+2Ca)/(Al\times Si)$] is the compositional proxy and in a general way, the solubility of Zr increase with $M$ regardless of the temperature. If $M$ is kept constant, Zr saturation increases with $T$ but, if Zr saturation is kept constant the temperature decreases with $M$ (Boehnke et al., 2013).

Gentio metagranitoid presents $M$ varying from 1.14 to 1.45. The higher temperature samples (~815 °C) are related to intermediate rocks (SiO$_2$ ~70 wt.%), with modal granodiorite composition, $M$ of 1.26–1.27, and Zr concentration of 273 ppm–275 ppm. On the other hand, the lowest temperature (714 °C) sample has higher SiO$_2$ content (~74%), and modal monzogranitic composition, $M$ of 1.14, and Zr concentration of 92 ppm. The lower $M$ values provide the lowest calculated $T_{Zr}$ however, the highest $T_{Zr}$ are not provided from the highest $M$ results.

We observe a considerable variation in Zr concentration between samples with the same $M$ values while, in most of the cases, no significant change in $M$ and $T$ values occurs when the sample has a similar Zr concentration. Considering that most samples of the Gentio metagranitoid present quartz and feldspar proportions close to near minimum-temperature melt compositions, we argue that the content of Zr of the source and not the

**Table 6**   U-Pb LA-ICP-MS zircon analytical data of Gentio's porphyritic facies. Sample and standard are corrected after Pb and Hg blanks

| Spot | Ratios | | | | | | | Th (ppm) | U (ppm) | Pb (ppm) |
| --- | --- | --- | --- | --- | --- | --- | --- | --- | --- | --- |
| | $^{207}Pb/^{235}U$ | % error | $^{206}Pb/^{238}Pb$ | % error | $\rho$ | $^{207}Pb*/^{206}Pb$ | % error | | | |
| Zr-36-A-V-01a | 7.104 83 | 1.78 | 0.387 35 | 0.71 | 0.96 | 0.133 03 | 1.63 | 197.2 | 240.9 | 119.4 |
| Zr-36-A-V-03 | 6.729 65 | 3.40 | 0.370 46 | 3.05 | 0.98 | 0.131 75 | 1.5 | 382.9 | 310.1 | 158.4 |
| Zr-36-A-V-05 | 7.233 66 | 2.49 | 0.391 70 | 2.06 | 0.94 | 0.133 94 | 1.4 | 44.3 | 161.3 | 119.1 |
| Zr-36-A-V-08 | 7.359 22 | 2.50 | 0.396 68 | 1.85 | 0.97 | 0.134 55 | 1.67 | 98.2 | 192.9 | 89.9 |
| Zr-36-A-V-09 | 7.054 65 | 2.14 | 0.384 65 | 1.46 | 0.93 | 0.133 02 | 1.57 | 385 | 350.3 | 188.1 |
| Zr-36-A-V-14 | 7.128 42 | 4.37 | 0.390 23 | 3.99 | 0.97 | 0.132 49 | 1.8 | 264.6 | 344.1 | 149 |
| Zr-36-A-V-18a | 7.047 45 | 2.43 | 0.388 65 | 1.92 | 0.98 | 0.131 51 | 1.48 | 182.7 | 188.4 | 95.1 |
| Zr-36-A-V-21 | 7.078 23 | 4.59 | 0.386 86 | 4.22 | 0.99 | 0.132 70 | 1.81 | 85.6 | 198.1 | 83.1 |
| Zr-36-A-V-24b | 6.819 03 | 3.21 | 0.375 34 | 2.73 | 0.99 | 0.131 76 | 1.7 | 95.2 | 295 | 116.5 |
| Zr-36-A-V-25 | 5.706 10 | 4.86 | 0.318 51 | 4.39 | 0.99 | 0.129 93 | 2.08 | 680.5 | 202.7 | 91.5 |
| Zr-36-A-VI-01 | 7.043 59 | 2.83 | 0.385 85 | 2.10 | 0.87 | 0.132 40 | 1.9 | 244.4 | 194.8 | 105.9 |
| Zr-36-A-VI-02 | 7.091 90 | 2.35 | 0.388 09 | 1.84 | 0.95 | 0.132 53 | 1.47 | 310.2 | 251.4 | 140 |
| Zr-36-A-VI-05 | 6.937 08 | 3.54 | 0.385 42 | 3.06 | 0.99 | 0.130 54 | 1.77 | 341.9 | 346.8 | 149.4 |
| Zr-36-A-VI-07 | 6.929 41 | 1.81 | 0.381 17 | 0.49 | 0.87 | 0.131 85 | 1.74 | 342.4 | 280.8 | 151 |
| Zr-36-A-VI-08 | 6.841 47 | 2.76 | 0.378 01 | 1.86 | 0.95 | 0.131 26 | 2.05 | 156 | 150.1 | 76.1 |
| Zr-36-A-VI-10 | 6.822 78 | 2.37 | 0.382 28 | 1.24 | 0.96 | 0.129 44 | 2.02 | 192.1 | 256.8 | 121.8 |
| Zr-36-A-VI-12 | 6.157 20 | 5.06 | 0.349 51 | 4.75 | 0.99 | 0.127 77 | 1.75 | 365.7 | 408.6 | 165.9 |
| Zr-36-A-VI-13 | 6.579 84 | 1.79 | 0.360 39 | 0.66 | 0.97 | 0.132 42 | 1.67 | 105.6 | 320.9 | 130.2 |
| Zr-36-A-VI-17 | 6.578 36 | 4.34 | 0.375 41 | 3.94 | 0.84 | 0.127 09 | 1.82 | 454.7 | 446.8 | 168.6 |
| Zr-36-A-VI-18 | 6.828 50 | 2.14 | 0.379 12 | 1.05 | 0.74 | 0.130 63 | 1.86 | 305.2 | 334.6 | 162.7 |
| Zr-36-A-VI-20 | 6.927 21 | 2.82 | 0.386 55 | 1.67 | 0.99 | 0.129 97 | 2.26 | 403.1 | 355 | 165 |
| Zr-36-A-VI-21 | 6.898 37 | 3.60 | 0.381 67 | 3.20 | 0.94 | 0.131 08 | 1.65 | 141.5 | 162.5 | 80.6 |
| Zr-36-A-V-04a* | 9.560 52 | 2.73 | 0.442 41 | 2.05 | 0.99 | 0.156 73 | 1.81 | 73.1 | 489.5 | 195.2 |
| Zr-36-A-VI-06* | 7.625 42 | 3.13 | 0.398 66 | 2.53 | 0.95 | 0.138 73 | 1.84 | 52.2 | 64.2 | 33.6 |
| Zr-36-A-V-06b** | 0.773 53 | 9.77 | 0.085 3 | 9.39 | 0.11 | 0.065 77 | 2.71 | 10 540.8 | 1 579.6 | 182.1 |
| Zr-36-A-V-12** | 0.974 22 | 2.82 | 0.108 44 | 1.62 | 0.26 | 0.065 16 | 2.31 | 613.6 | 3 208.9 | 286.2 |
| Zr-36-A-V-15** | 0.853 75 | 6.75 | 0.095 43 | 6.14 | 0.65 | 0.064 88 | 2.81 | 300.6 | 3 288.2 | 475.7 |

**Table 6**  Continued

| Spot | Ages (Ma) | | | | | | Disc. % | % common Pb | $^{232}$Th/$^{238}$U |
|---|---|---|---|---|---|---|---|---|---|
| | $^{206}$Pb/$^{238}$U | % error | $^{207}$Pb/$^{235}$U | ± | $^{207}$Pb/$^{206}$Pb | % error | | | |
| Zr-36-A-V-01a | 2 111 | 15 | 2 125 | 38 | 2 138 | 35 | 1 | 0.000 4 | 0.82 |
| Zr-36-A-V-03 | 2 032 | 62 | 2 077 | 71 | 2 121 | 32 | 4 | 0.000 5 | 1.24 |
| Zr-36-A-V-05 | 2 131 | 44 | 2 141 | 53 | 2 150 | 30 | 1 | 0.001 1 | 0.28 |
| Zr-36-A-V-08 | 2 154 | 40 | 2 156 | 54 | 2 158 | 36 | 0 | 0.000 5 | 0.51 |
| Zr-36-A-V-09 | 2 098 | 31 | 2 118 | 45 | 2 138 | 34 | 2 | 0.000 3 | 1.11 |
| Zr-36-A-V-14 | 2 124 | 85 | 2 128 | 93 | 2 131 | 38 | 0 | 0.000 9 | 0.77 |
| Zr-36-A-V-18a | 2 117 | 41 | 2 117 | 51 | 2 118 | 31 | 0 | 0.000 6 | 0.98 |
| Zr-36-A-V-21 | 2 108 | 89 | 2 121 | 97 | 2 134 | 39 | 1 | 0.001 9 | 0.43 |
| Zr-36-A-V-24b | 2 054 | 56 | 2 088 | 67 | 2 122 | 36 | 3 | 0.000 9 | 0.33 |
| Zr-36-A-V-25 | 1 782 | 78 | 1 932 | 94 | 2 097 | 44 | 15 | 0.005 5 | 3.38 |
| Zr-36-A-VI-01 | 2 104 | 44 | 2 117 | 60 | 2 130 | 40 | 1 | 0.001 2 | 1.26 |
| Zr-36-A-VI-02 | 2 114 | 39 | 2 123 | 50 | 2 132 | 31 | 1 | 0.000 5 | 1.24 |
| Zr-36-A-VI-05 | 2 102 | 64 | 2 103 | 74 | 2 105 | 37 | 0 | 0.001 9 | 0.99 |
| Zr-36-A-VI-07 | 2 082 | 10 | 2 102 | 38 | 2 123 | 37 | 2 | 0.000 3 | 1.23 |
| Zr-36-A-VI-08 | 2 067 | 38 | 2 091 | 58 | 2 115 | 43 | 2 | 0.000 7 | 1.05 |
| Zr-36-A-VI-10 | 2 087 | 26 | 2 089 | 49 | 2 090 | 42 | 0 | 0.000 9 | 0.75 |
| Zr-36-A-VI-12 | 1 932 | 92 | 1 998 | 101 | 2 067 | 36 | 7 | 0.001 2 | 0.9 |
| Zr-36-A-VI-13 | 1 984 | 13 | 2 057 | 37 | 2 130 | 35 | 7 | 0.001 1 | 0.33 |
| Zr-36-A-VI-17 | 2 055 | 81 | 2 056 | 89 | 2 058 | 38 | 0 | 0.004 8 | 1.03 |
| Zr-36-A-VI-18 | 2 072 | 22 | 2 089 | 45 | 2 106 | 39 | 2 | 0.000 6 | 0.92 |
| Zr-36-A-VI-20 | 2 107 | 35 | 2 102 | 59 | 2 098 | 47 | 0 | 0.000 8 | 1.14 |
| Zr-36-A-VI-21 | 2 084 | 67 | 2 098 | 76 | 2 113 | 35 | 1 | 0.000 6 | 0.88 |
| Zr-36-A-V-04a* | 2 361 | 48 | 2 393 | 65 | 2 421 | 44 | 2 | 0.007 0 | 0.15 |
| Zr-36-A-VI-06* | 2 163 | 55 | 2 188 | 68 | 2 211 | 41 | 2 | 0.001 7 | 0.82 |
| Zr-36-A-V-06b** | 528 | 50 | 582 | 57 | 799 | 22 | 34 | 0.128 2 | 6.72 |
| Zr-36-A-V-12** | 664 | 11 | 691 | 19 | 779 | 18 | 15 | 0.006 0 | 0.19 |
| Zr-36-A-V-15** | 588 | 36 | 627 | 42 | 771 | 22 | 24 | 0.130 9 | 0.09 |

All errors in the table are calculated 1σ (% for isotope ratios, absolute for ages). [a]. Corrected to common lead ($^{204}$Pb); *. inherited zircon; **. metamorphic zircon.

**Table 7**   Sm-Nd analytical data of Gentio metagranitoid

| Samples | Detail | Sm (ppm) | Nd (ppm) | $^{147}Sm/^{144}Nd$ | Error | $^{143}Nd/^{144}Nd$ | Error | $\varepsilon_{(0)}$ | $f_{Sm/Nd}$ | $T_{DM}$ (Ma) | $T_i$ (Ma) | $\varepsilon_{Nd}(2.1)$ |
|---|---|---|---|---|---|---|---|---|---|---|---|---|
| MA-25A | Porphyritic facies | 4.082 | 28.670 | 0.086 1 | 0.000 5 | 0.511 070 | 0.000 008 | -30.56 | -0.56 | 2 364 | 2 120 | -0.7 |
| MA-24A | Equigranular facies | 3.520 | 17.780 | 0.119 7 | 0.000 7 | 0.511 350 | 0.000 007 | -25.14 | -0.39 | 2 773 | 2 111 | -4.4 |
| MA-73C | Equigranular facies | 4.840 | 36.197 | 0.080 9 | 0.000 5 | 0.510 760 | 0.000 006 | -36.63 | -0.59 | 2 636 | 2 111 | -5.4 |
| MA-89F | Equigranular facies | 4.938 | 30.824 | 0.096 9 | 0.000 6 | 0.511 130 | 0.000 008 | -29.44 | -0.51 | 2 511 | 2 111 | -2.6 |
| MA-25C | Equigranular facies | 4.111 | 27.035 | 0.092 0 | 0.000 5 | 0.511 070 | 0.000 008 | -30.56 | -0.53 | 2 481 | 2 111 | -2.4 |
| MA-73D1 | Equigranular facies | 4.331 | 28.034 | 0.093 4 | 0.000 5 | 0.511 110 | 0.000 009 | -29.75 | -0.53 | 2 458 | 2 111 | -2 |
| NAT-38 | Equigranular facies | 2.390 | 18.100 | 0.079 8 | 0.004 4 | 0.511 040 | 0.000 008 | -31.17 | -0.55 | 2 437 | 2 111 | -1.9 |
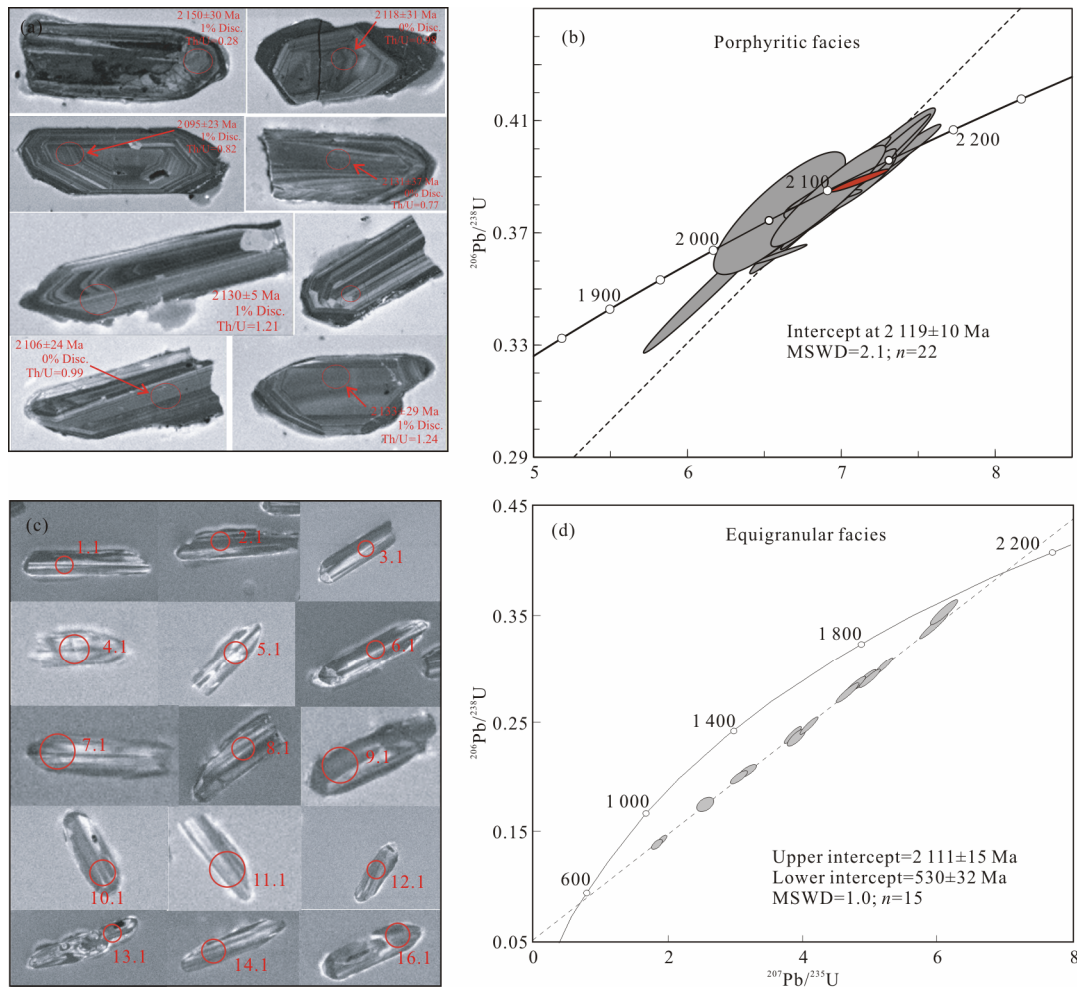


**Figure 9.** (a) Cathodoluminescence images of selected zircon grains of the porphyritic facies analyzed by LA-ICP-MS and (b) U-Pb concordia diagram. (c) Cathodoluminescence images of selected zircon grains from the equigranular facies analyzed by SHRIMP (red label are the spot numbers) and (d) U-Pb concordia diagram.

initial melt composition was the main controller of the Zr concentration. Boehnke et al. (2013) predict that at 750 °C and $M$ of 1.41, 800 °C and $M$ of 1.36, zircon solubility achieves values of 206 ppm (±30) and 155 ppm (±30), respectively. Those values are comparable to the ones from the Gentio metagranitoid.

The LA-ICP-MS analyses indicated only two zircon grains showing calculated age inheritance in the porphyritic facies sample, while no inherited zircon grain was detected in the sample of the equigranular facies. Additionally, zircon grains are euhedral, present pronounced internal zoning and occur as inclusion in the early crystallized minerals phases like plagioclase and biotite, implying that it was an earlier melt-precipitated phase. Thus, we assume that for most of the studied samples, the magma was

saturated in Zr at the source, so that the calculated $T_{Zr}$ may represent the temperature close to the true value.

### 4.2   Water Content

The Gentio metagranitoid corresponds to an I-type rock as evidenced by the presence of igneous accessory minerals such as titanite and allanite, absence of primary Al-rich minerals (e.g., muscovite, cordierite, sillimanite, and kyanite). Additionally, biotite from the studied body is moderately enriched in Mg and falls into the field of I-type granites in the ternary diagrams (Figs. 7a and 7b) of Nockolds (1947) and Abdel-Rahman (1994).

The most efficient mechanism for generating a significant volume of granitoid magma is partial melting of older crustal
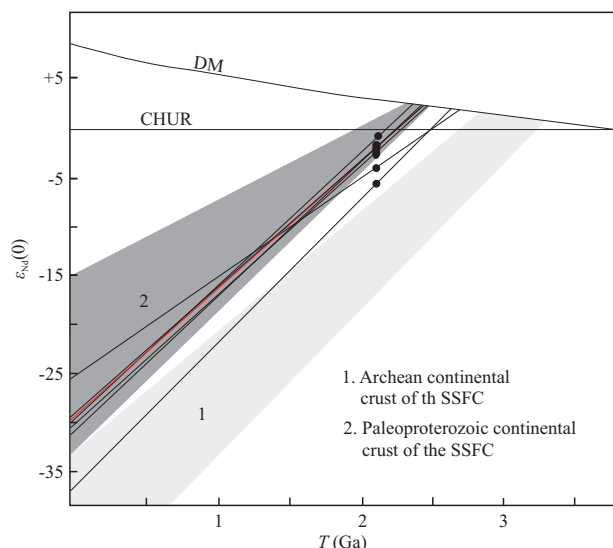
**Figure 10.** The Nd evolution vs. time (crystallization ages) diagram for Gentio metagranitoid samples. The isotopic field of the Archean (1) and Paleoproterozoic (2) refers to analyses of the basement of the South of the São Francisco Craton compiled from Ávila et al. (2010) and Barbosa et al. (2015). The sample from the low-SiO$_2$ group is in red.

lithologies that can occur under the presence or absence of water. If a free fluid phase is not available, partial melting of igneous rocks occurs by dehydration melting of biotite and amphibole, and several studies have demonstrated that this process requires higher temperatures (>800 °C) (e.g., Patiño Douce and McCarthy, 1998; Patiño Douce and Beard, 1995; Clemens and Vielzeuf, 1987).

If free water is available, granitic magma may form at a temperature as low as 625 °C (see Luth et al., 1964). Wet partial melting is a common process (e.g., Weinberg and Hasalová, 2015; Thompson and Connolly, 1995; Whitney, 1988 and references therein). The water-saturated granite solidus temperature decreases by 200 °C if dissolved H$_2$O increases from 0 to 2 wt.% (Holtz et al., 2001). Studies in metamorphic terranes identified high degrees of partial melting occurred due to fluid infiltration at low temperature, ~700 °C (Sawyer et al., 2011). The origin of the water could be from dehydration reactions in nearby metasedimentary rocks, from crystallizing plutons, meteoric water, or from the mantle. Major crustal-scale shear zones can also provide the pathways for the H$_2$O to infiltrate the continental crust (Sawyer et al., 2011). At upper amphibolite facies, water-fluxed melting will typically cause congruent melting and form minimum melts (Weinberg and Hasalová, 2015).

Low-temperature granitoid is likely felsic and present eutectic (or near eutectic) composition characterized by more than 80% normative abundances of quartz, albite, and orthoclase (Tuttle and Bowen, 1958). According to Holtz et al. (2001) eutectic melt is necessarily water-rich (5 wt.% H$_2$O). We argue that additional low-temperature indicators may include preservation of whole-rock heterogeneous chemical compositions as observed in the Gentio metagranitoid.

The amount of water in geological material is often expressed in terms of weight percent and/or water activity. Holtz et al. (2001) determined the maximum water contents that can

be dissolved in a granitic melt at different $P$-$T$-$a_{H_2O}$. They showed that, once water is available, its solubility is mainly a function of pressure and, at 2 kbar the highest water contents that can be incorporated into the melt is 6 wt.%, while at 5 kbar this value increases to 10 wt.%. In both cases, the $a_{H_2O}$ is equal to 1.0 and thus, the melt is saturated in water.

Johannes and Holtz (1996) showed that partial melting under the presence of water can produce a large volume of unsaturated melt. For instance, if a melt is generated at 5 kbar under the presence of 5 wt.% of H$_2$O and undergone isobaric heating, the ratio of water/melt would decrease as the temperature increase. In this situation, if the temperature changes from 640 to 700 °C, 50% of the melt is generated under $a_{H_2O}$ of 0.7. Thus, the melt would be capable of rising to shallow crustal levels (3 to 2 kbar).

In the ternary diagram with the CIPW normative Or+Ab+Qz content of the Gentio metagranitoid, the samples from the high-SiO$_2$ group are aligned along or close to the eutectic curve (Fig. 11). The low-SiO$_2$ group plots on the left side of the diagram (samples in red) and presents the lowest K$_2$O concentrations (1.9 wt.%–2.1 wt.%) and the highest CaO content (3.8 wt.%–4.3 wt.%) and FeO$_T$+MgO between 5.6 wt.% and 6.3 wt.%. We propose that those samples were either formed from a source depleted in the Or component and/or under high $a_{H_2O}$. At high $a_{H_2O}$, melts become richer in Ab and poorer in Or component (Johannes and Holtz, 1996). Additionally, for low H$_2$O contents biotite is the last mineral to crystallize, and for higher H$_2$O contents crystallization of biotite precedes that of alkali feldspar and quartz (Maaløe and Wyllie, 1975).

Considering the Gentio metagranitoid chemical composition and mineralogy (modal and normative) and comparing with experimental data (Fig. 11), we speculate that the different magmatic pulses were formed under a variety of $a_{H_2O}$, probably
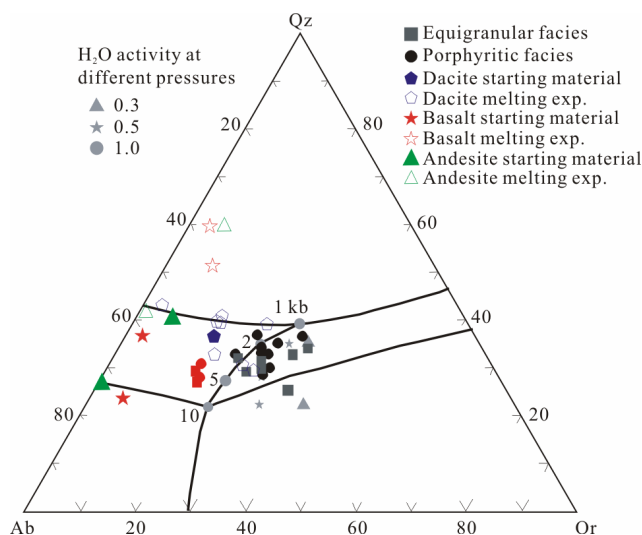


**Figure 11.** Ternary quartz-albite-orthoclase diagram from the Gentio metagranitoid and experimental data. Dacite data from Conrad et al. (1988). Basalt and andesite data from Beard and Lofgren (1991). The cotectic lines and H$_2$O-saturated minimum and eutectic melt compositions data are from Ebadi and Johannes (1991), Holtz and Johannes (1991), Holtz et al. (1989), Luth et al. (1964), and Tuttle and Bowen (1958). The red square and circle belong to the low SiO$_2$ group. See text for details.

between 0.4 and 0.8. This range of values for the water activity is considered here taking into account two important points: (1) The importance of the minimum amount of water needed to melt completely a quartz-alkali feldspar assemblage, that at a constant temperature, this minimum water content increases with increasing pressure (Johannes and Holtz, 1996). (2) The felsic nature of the studied body. The Qz content decreases with increasing pressure thus, partial melting at great depths (20 kbar) is not granitic but syenitic or quartz-syenitic in composition (Johannes and Holtz, 1996).

### 4.3   Sources Rocks of the Gentio Metagranitoid

To offer source constraints and to evaluate the "fertility" of some igneous rock to generate granitic magma under low-temperature conditions (≤800 °C) and in the presence of water, we compared major element compositions of the Gentio meta-granitoid with experimental data performed using juvenile and more evolved igneous rock (natural composition). Due to the

limited number of experimental studies that fulfill those conditions, we use only two references: Conrad et al. (1988) and Beard and Lofgren (1991).

The experiments from Beard and Lofgren (1991) were performed under water-saturated conditions ($a_{H_2O}$=1) at 7 kbar and temperature of 800 °C, while the experiments of Conrad et al. (1988) were run with water activity between 0.25 and 1, the pressure of 7 kbar, and temperature of 675–825 °C.

In the Harker diagrams, the starting material of dacitic composition (Conrad et al., 1988) presents $SiO_2$, $TiO_2$, $FeO_T$, and $K_2O$ contents similar to the low-$SiO_2$ group of the Gentio metagranitoid. Conversely, basalts and andesites studied by Beard and Lofgren (1991) are very different in all elements (Fig. 12). The basalt and andesite starting materials produced melt richer in $Al_2O_3$ (Fig. 12), more peraluminous (Fig. 7b), and with lower $K_2O$ content (Fig. 7a) than the compositions of the Gentio metagranitoid. However, some runs resulting from dacite compositions presented $Al_2O_3$, $CaO$, $Na_2O$, and $K_2O$
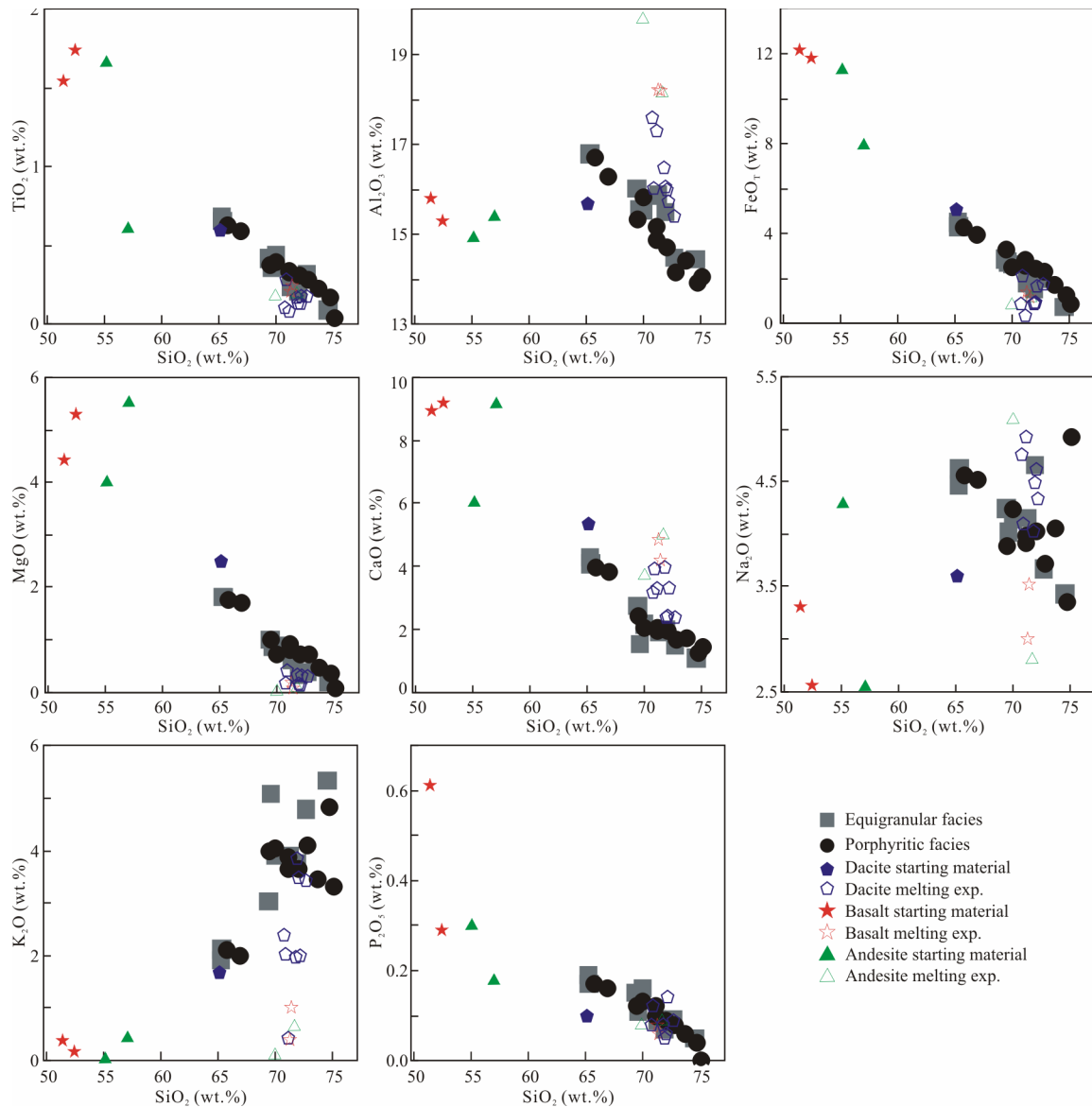


**Figure 12.** Harker variation diagrams for major elements from the Gentio metagranitoid and experimental data. Dacite data from Conrad et al. (1988); basalt and andesite data from Beard and Lofgren (1991). See text for details.

contents comparable to the high-SiO$_2$ group (Figs. 7 and 12). For the P$_2$O$_5$ content, we observed an overlap between all runs, even though the compositions of basalts and andesites starting materials exhibit higher initial P$_2$O$_5$ values and produced more peraluminous melt compared to the dacites. Considering only MgO, FeO$_T$, and TiO$_2$ content, we observe a similar behavior regarding the source rock, with most samples exhibiting concentrations slightly lower than the high-SiO$_2$ group of the Gentio metagranitoid (Fig. 12).

Melts resulting from partial melting of basalt and andesite starting materials plot in the tholeiitic series and preclude producing calc-alkaline to the high-K calc-alkaline rocks (Fig. 7a). On the other hand, the dacite starting material produced melts that plot in the field of calc-alkaline and high-K calc-alkaline series (Fig. 7a) similar to the high-SiO$_2$ group. The samples with higher K$_2$O content are the ones with $a_{H_2O}$ varying between 0.25 and 0.5.

Beard and Lofgren (1991) demonstrated that basalt, even under saturated conditions, was not able to generate a considerable amount of melt under low-temperature conditions. Their results showed that while andesite starting material produced 44%–55% melt at 800 °C and 6.9 kbar basalts only generated 27%–29% of melt.

In the Ab-Qz-Or ternary diagram, we observed that all samples resulted from experiments performed under water-saturated condition ($a_{H_2O}$=1) produced melt of tonalite and granodiorite normative composition, and did not produce melt near to the haplogranitic eutectic composition (Fig. 11). The two samples overlapping the high-SiO$_2$ group of the Gentio metagranitoid exhibit water activity of 0.5 and temperatures between 725 and 750 °C. On the other hand, the sample that plots closer to the low-SiO$_2$ group presents water activity of 0.75 and temperature of 725 °C.

The experimental data showed that when there is the availability of a certain element, its behavior will be controlled by the melting conditions. The Gentio metagranitoid exhibits great variation in SiO$_2$ (65 wt.% to 76 wt.%) and FeO$_T$+MgO content (0.9 wt.% to 6.3 wt.%). Considering only the high-SiO$_2$ group we observe that the higher calculated $T_{Zr}$ samples (760–815 °C) are more mafic than the lower calculated $T_{Zr}$ samples (720–740 °C), suggesting that the temperature may have controlled the amount of mafic component that has entered the melt.

The chondrite-normalized REE diagrams show enrichment in LREE in comparison to HREE. Allanite, when present, is the main responsible phase for the LREE concentration in I-type granite while garnet and not zircon is the main responsible phase to concentrate HREE (Bea, 1996; Pimentel and Charnley, 1991). The Gentio metagranitoid presents igneous allanite and zircon thus, we propose two possibilities to explain the observed REE pattern: (i) the source rocks were enriched in LREE and depleted in the HREE phases, and/or (ii) the source rocks contained enough HREE-rich minerals, but they were probably retained in the residue after partial melting. Even though the REE pattern does not vary greatly among all samples, the Eu anomaly ranges from slightly positive to negative (Figs. 8a and 8b), since no fractionation process could account for this behavior. We argue that the availability of this element

in the source region together with the $f_{O_2}$ during partial melting has controlled the observed heterogeneity.

We conclude that the source rocks' composition and processes operating during partial melting (e.g., changes in $P$-$T$-$a_{H_2O}$) were the most important parameters controlling the chemical compositional heterogeneity observed in the studied pluton. The variable Sm-Nd isotopic signatures suggest that different source rocks and/or a source with heterogeneous composition contributed to its formation. The negatives $\varepsilon_{Nd(i)}$ values coupled with the crustal-like signatures (Weaver and Tarney, 1984) of the primitive average crust-normalized diagram (Figs. 8c and 8d) reinforce an origin from the recycling of a more evolved Archean/Paleoproterozoic crustal material.

The Gentio metagranitoid is intrusive into amphibolites with a tholeiitic affinity of the Dores de Campos metavolcanic-sedimentary sequence (2.26 Ga, Ávila et al., 2012) and it is spatially associated with the Brejo Alegre tonalitic orthogneiss (2 166±5 Ma, Silva et al., 2020) and the Vitoriano Veloso metagabbro. The first one is a small elongated body while the second is a pluton with tholeiitic affinity. Since the generation of the studied body requires a more evolved Paleoproterozoic and Archean crustal source material (older calc-alkaline to high-K calc-alkaline granitoid, dacite, or andesite) which was not recognized in terms of volume, composition, and age in the region yet or maybe the restite was retained in depth while the melt was transported to a shallower level in the crust.

### 4.4　Pluton Construction and Evolution

Field evidence of multiple magma injections related to the equigranular rocks is preserved in the pluton in the outcrop scale (Fig. 2a). For the porphyritic facies, field evidence for multiple magma batches is not so obvious, even though the same chemical and compositional heterogeneity are observed (Figs. 6, 7, and 8).

In our model (Fig. 13), the porphyritic rocks were the first to emplace and the batches build a magma reservoir. The lack of sharp contact between the multiples injections of the porphyritic facies may be explained by an interplay between emplacement styles and emplacement rates of the magma bodies (Annen, 2011) and/or because the batches were emplaced in a melt-bearing magma reservoir (e.g., Farina et al., 2012; Miller et al., 2011).

The variety of calculated $T_{Zr}$ obtained from the samples indicates different episodes of reheating. Higgins (1999) proposed that the formation of K-feldspar phenocrysts would be associated with the dissolution of smaller crystals to feed the growth of larger ones, whereas Johnson and Glazner (2010) suggested that the development of alkali-feldspar phenocrysts can be explained by temperature oscillation. Mills and Glazner (2013) demonstrated that oscillation of the temperature is a very efficient mechanism for the growth of olivine and plagioclase crystals in alkaline basalts under atmospheric pressure and temperatures of 1 150 °C. Silva et al. (2017) applied this methodology in a rhyolitic system under pressures of 1 and 2 kbar and temperatures between 725 and 815 °C and demonstrated that the growth of amphibole and plagioclase is significantly affected by temperature oscillations of ±15 °C. As temperature oscillation was common during the formation of the Gentio metagranitoid due to the repeated injections of new
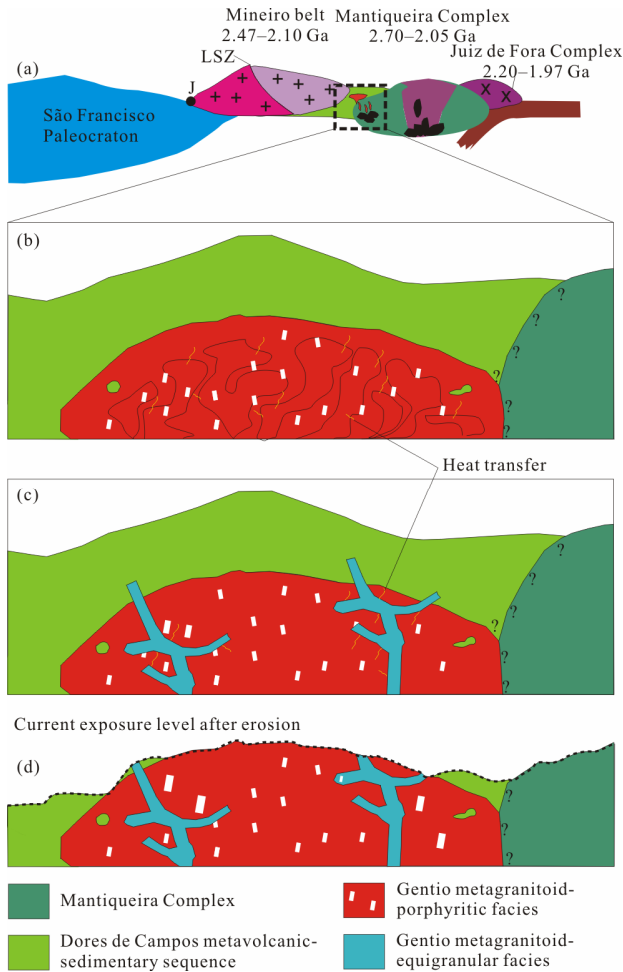
**Figure 13.** Schematic model of the tectonic evolution of the Mineiro belt and Mantiqueira Complex illustrating the emplacement of the Gentio metagranitoid in a post-collisional environment (adapted from Ávila et al., 2010; Heilbron et al., 2010). (a) Sketch of the collision of São Francisco Paleocraton with the Mineiro belt and Mantiqueira and Juiz de Fora complexes. (b) Different batches of the magmas related to the porphyritic facies were the first to emplaced. Increments may happen simultaneously causing different episodes of reheating which explain the presence and the size of feldspar phenocrysts. (c) The equigranular rocks were emplaced into a crystal-rich porphyritic reservoir and maybe also contributed to the growth of the phenocrysts. (d) Arc erosion and current exposure of the Gentio metagranitoid and the different rocks of the Dores de Campos metavolcanic-sedimentary sequence. See the text for more details. LSZ. Lenheiro shear zone; J. Jeceaba-Bom Sucesso lineament; DCMSS. Dores de Campos metavolcanic-sedimentary sequence.

batches of hotter magma, this could explain the presence of phenocrysts and porphyritic texture.

Gentio metagranitoid present phenocrysts of plagioclase and a smaller amount of K-feldspar that grew early and simultaneously, since we can find inclusions of these minerals into each other. Experimental studies indicate that when K-feldspar begins to crystallize in granites, the magma typically contains of 60% to 70% liquid (Vernon and Paterson, 2008; Clemens and Wall, 1981) and this is in agreement with the studied body.

Individual magma batches were subject to little or no fractionation process during crystallization. Fractional crystallization is the process by which a crystal separates from its melt

leading to progressive changes in that melt composition. In an ideal case, a suite that was differentiated by this process should present field, mineralogy, and chemical evidence for fractionation. For example, zoned pluton with a coherent magmatic sequence from early mafic to intermediate parent magmas to late felsic fractionated granite. Chemically, a group of genetically related mafic to felsic rocks should form tight and coherent arrays on Harker diagrams (Clemens et al., 2009).

The more mafic rocks belong to the low-$SiO_2$ group and present biotite as the only mafic mineral and together with plagioclase were the first major phases in the crystallization sequence. The high-$SiO_2$ group has Eu/Eu*, Rb, Sr, and Ba contents that rule out plagioclase as the fractionated mineral, since those elements concentration do not exhibit a coherent variation with maficity, and $SiO_2$ content. Biotite and minor early crystallized phases such as zircon, titanite, allanite cannot have controlled any fractionation processes because an enormous degree of fractionation of any of these phases would be required to explain the observed major and trace elements behavior in the high-$SiO_2$ group.

Another important piece of evidence that argues against fractional crystallization is the variation of the $K_2O$ vs. $SiO_2$ content (Fig. 7a) in the diagram proposed by Peccerillo and Taylor (1976). The samples from Gentio metagranitoid exhibit a considerable degree of scattering and plot in two different fields of this diagram: the calc-alkaline and the high-K calc-alkaline series with a gap between the two groups of samples, reinforcing that there is no evolutive relation between them. Furthermore, to move into adjacent field, processes other than crystal-liquid separation must operate (Roberts and Clemens, 1993), for example, a different rate of partial melting controlled by a change in $P$-$T$-$a_{H_2O}$ during anatexis.

Features such as: (i) absence of hybrid rock, (ii) presence of well-preserved mafic xenoliths (Fig. 2b) not exhibiting evidence of chemical interaction with the host rock, and (iii) lack of disequilibrium textures, indicate that no significant change in melt composition has occurred during its crystallization. Wherefore, eliminates magma mixing with a mafic source as responsible for the diversity of chemical compositions observed. Besides, the low-calculated $T_{Zr}$ of the studied body advocates against this process.

The presence of partly disaggregated mafic enclaves (Fig. 2e) are rare and limited to a small portion of the pluton and even if partial assimilation of the host rock has occurred, is restricted to small-scale (millimetric) event. One may question if mixing between the different batches may have occurred but, there is no direct evidence to support it.

## 4.5 Tectonic Settings

There have been several attempts to categorize granitoid according to the geotectonic environments into which they were generated. Tectonic-discriminant diagrams use geochemical parameters (major or trace elements) as indicative of tectonic settings assuming that geochemical characteristics will reflect source composition and certain combinations of sources are more likely to occur in a specific tectonic environment, so the chemical composition will also characterize the tectonic setting. However, this assumption is unsuitable for granitoid,

because they are the product of recycling older lithologies, and the compositions of the low-temperature ones, regardless its source rocks (igneous and/or sedimentary), converge towards minimum-temperature melt composition.

Pearce et al. (1984) proposed a widely used scheme to classify granitoid according to their tectonic environment. Condie (2015) and Moyen and Laurent (2018) pointed out many problems using this oversimplified tectonomagmatic connection including (i) mantle sources can be present in many tectonic settings and even if a source rock was formed during a subduction process, it can subsequently be involved in a continental collision; (ii) degree of partial melting, differentiation and post magmatic process can affect incompatible element distributions thus, depending on the extent of those process, the resulted rock may not reflect its source; (iii) Archean geodynamic was different from modern tectonic processes, thus, the use of discrimination diagrams based on modern magmas is meaningless for Archean terrains and the rocks resulted from the partial melting of Archean lithologies. Additionally, the mentioned discriminant diagram is unsuitable for crustal granitoid or for rock with a major contribution from crustal lithologies (see Pearce, 1996).

The Gentio metagranitoid preserves its primary features and is much less deformed than the surrounding rocks that were metamorphosed under amphibolite facies. Thus, a regional deformational-metamorphic event occurred before its emplacement, between 2.17 and 2.13 Ga. Field evidence suggests that the Gentio metagranitoid was emplaced in a preexisting weak zone (possibly an older shear zone) which controlled and facilitated the creation of space in a late-stage tectonic activity. Post-magmatic structures observed in the studied body are likely related to the Brasiliano orogeny as they also affected the rocks of the younger Carandaí megasequence (>1 379±3 Ma, Ribeiro et al., 2013) that covers part of the Gentio metagranitoid and were metamorphosed between 604 and 567 Ma (Ribeiro et al., 2013 and references therein). Metamorphic ages of 659±43 and 530±32 Ma were recognized in homogeneous zircon grains from the studied body.

Therefore, we argue that the most plausible geodynamic environment to explain the genesis of the Gentio metagranitoid is a post-collisional environment, after the amalgamation of the Mineiro belt and the Mantiqueira Complex. However, a suture indicating the exact boundary between these two major units was not yet recognized and more detailed mapping in the south/southeast region of the studied body is necessary.

## 5  CONCLUSIONS

The Gentio metagranitoid is intrusive in amphibolites and metaultramafic rocks of the Dores de Campos metavolcanic-sedimentary sequence and it was formed through several magmatic pulses. It corresponds to a low temperature (≤800 °C) I-type granite, characterized by large heterogeneity about its textural features, modal, chemical, and isotopic composition. The individual batches were submitted subject to little or no fractionation process after their emplacement and the observed heterogeneity within batches was attributed mainly to: (i) inheritance from the source rock; (ii) variable $P$-$T$-$a_{H_2O}$ conditions during partial melting.

Its source rocks were older igneous and/or metaigneous quartz-feldspathic rocks, intermediate to felsic, calc-alkaline to high-K calc-alkaline (e.g., granitoid, dacite, andesite) that were melted in presence of a hydrous phase. Given its crystallization age—2 119±10 and 2 111±15 Ma—the Gentio metagranitoid represents the final evolutionary stage of the Mineiro belt and was formed in a post-collisional environment, after the accretion of the Mantiqueira Complex with the Mineiro belt. We propose that the collision between these two units may have occurred between 2.17 and 2.13 Ga. This range of ages is older than the previous interval of 2.10–2.05 Ga proposed by Teixeira et al. (2015) and the age of 2.09 Ga pointed by Barbosa et al. (2015) as the collision age of the Mineiro belt with the Archean–Paleoproterozoic foreland (Minas Supergroup) along the Bom Sucesso-Jeceaba lineament. The primary mineralogy and textures of the Gentio metagranitoid were modified by a metamorphic event with ages between 659±43 and 530±32 Ma associated with the Brasiliano orogeny.

## REFERENCES CITED

Abdel-Rahman, A. F. M., 1994. Nature of Biotites from Alkaline, Calc-Alkaline, and Peraluminous Magmas. *Journal of Petrology*, 35(2): 525–541. https://doi.org/10.1093/petrology/35.2.525

Alkmim, F. F., Teixeira, W., 2017. The Paleoproterozoic Mineiro Belt and the Quadrilátero Ferrífero. In: Heilbron, M., Cordani, U., Alkmim, F., eds., São Francisco Craton, Eastern Brazil: Tectonic Genealogy of a Miniature Continent (Regional Geology Reviews). Springer. 45–62. https://doi.org/10.1007/978-3-319-01715-0_5

Annen, C., 2011. Implications of Incremental Emplacement of Magma Bodies for Magma Differentiation, Thermal Aureole Dimensions, and Plutonism-Volcanism Relationships. *Tectonophysics*, 500(1–4): 3–10. https://doi.org/10.1016/j.tecto.2009.04.010

Ávila, C. A., Bezerra Filho, A. P., Oliveira, N. D. B., et al., 2006a. Resultados Preliminares da Geologia do Quartzo Diorito Dores do Campo, Região de Tiradentes—Dores do Campo, Estado de Minas Gerais. In: XLIII Congresso Brasileiro de Geologia, Aracaju. 1: 183 (in Portuguese)

Ávila, C. A., Teixeira, W., Cordani, U. G., et al., 2006b. The Glória Quartz-Monzodiorite: Isotopic and Chemical Evidence of Arc-Related Magmatism in the Central Part of the Paleoproterozoic Mineiro Belt, Minas Gerais State, Brazil. *Anais da Academia Brasileira de Ciencias*, 78(3): 543–556. https://doi.org/10.1590/s0001-37652006000300013

Ávila, C. A., Teixeira, W., Cordani, U. G., et al., 2010. Rhyacian (2.23–2.20 Ga) Juvenile Accretion in the Southern São Francisco Craton, Brazil:

Geochemical and Isotopic Evidence from the Serrinha Magmatic Suite, Mineiro Belt. *Journal of South America Earth Sciences*, 29(2): 464–482. https://doi.org/10.1016/j.jsames.2009.07.009

Ávila, C. A., Teixeira, W., Vasques, F. S. G., et al., 2012. Geoquímica e Idade U-Pb (LA-ICPMS) da Crosta Oceânica Riaciana do Cinturão Mineiro, Borda Meridional do Cráton São Francisco. *Anais do Congresso Brasileiro de Geologia*, 46: 4–5

Ávila, C. A., Teixeira, W., Bongiolo, E. M., et al., 2014. Rhyacian Evolution of Subvolcanic and Metasedimentary Rocks of the Southern Segment of the Mineiro Belt, São Francisco Craton, Brazil. *Precambrian Research*, 243(4): 221–251. https://doi.org/10.1016/j.precamres.2013.12.028

Barbosa, N. S., Teixeira, W., Ávila, C. A., et al., 2015. 2.17–2.10 Ga Plutonic Episodes in the Mineiro Belt, São Francisco Craton, Brazil: U-Pb Ages, Geochemical Constraints and Tectonics. *Precambrian Research*, 270: 204–225. https://doi.org/10.1016/j.precamres.2015.09.010

Barbosa, N. T., Teixeira, W., Ávila, C. A., et al., 2019. U-Pb Geochronology and Coupled Hf-Nd-Sr Isotopic-Chemical Constraints on the Cassiterita Orthogneiss (2.47 to 2.41 Ga) in the Mineiro Belt, São Francisco Craton: Geodynamic Fingerprints beyond the Archean-Paleoproterozoic Transition. *Precambrian Research*, 326: 399–416. https://doi.org/10.1016/j.precamres.2018.01.017

Bea, F., 1996. Controls on the Trace Element Composition of Crustal Melts. *Special Paper of the Geological Society of America*, 315: 33–41. https://doi.org/10.1130/0-8137-2315-9.33

Beard, J. S., Lofgren, G. E., 1991. Dehydration Melting and Water-Saturated Melting of Basaltic and Andesitic Greenstones and Amphibolites at 1, 3, and 6.9 kb. *Journal of Petrology*, 32(2): 365–401. https://doi.org/10.1093/petrology/32.2.365

Black, L. P., Kamo, S. L., Allen, C. M., et al., 2003. TEMORA 1: A New Zircon Standard for Phanerozoic U-Pb Geochronology. *Chemical Geology*, 200(1/2): 155–170. https://doi.org/10.1016/s0009-2541(03)00165-7

Boehnke, P., Watson, E. B., Trail, D., et al., 2013. Zircon Saturation Re-Revisited. *Chemical Geology*, 351: 324–334. https://doi.org/10.1016/j.chemgeo.2013.05.028

Cardoso, C. D., Ávila, C. A., Neumann, R., et al., 2019. A Rhyacian Continental Arc during the Evolution of the Mineiro Belt, Brazil: Constraints from the Rio Grande and Brumado Metadiorites. *Lithos*, 326/327: 246–264. https://doi.org/10.1016/j.lithos.2018.12.025

Clemens, J. D., Wall, V. J., 1981. Origin and Crystallization of some Peraluminous (S-Type) Granitic Magmas. *Canadian Mineralogist*, 19(1): 111–131

Clemens, J. D., Vielzeuf, D., 1987. Constraints on Melting and Magma Production in the Crust. *Earth and Planetary Science Letters*, 86(2–4): 287–306. https://doi.org/10.1016/0012-821x(87)90227-5

Clemens, J. D., Helps, P. A., Stevens, G., 2009. Chemical Structure in Granitic Magmas—A Signal from the Source?. *Special Paper of the Geological Society of America*, 472: 159–172. https://doi.org/10.1130/2010.2472(11)

Condie, K., 2015. Changing Tectonic Settings through Time: Indiscriminate Use of Geochemical Discriminant Diagrams. *Precambrian Research*, 266: 587–591. https://doi.org/10.1016/j.precamres.2015.05.004

Conrad, W. K., Nicholls, I. A., Wall, V. J., 1988. Water-Saturated and -Undersaturated Melting of Metaluminous and Peraluminous Crustal Compositions at 10 kb: Evidence for the Origin of Silicic Magmas in the Taupo Volcanic Zone, New Zealand, and Other Occurrences. *Journal of Petrology*, 29(4): 765–803

DePaolo, D. J., 1981. A Neodymium and Strontium Isotopic Study of the Mesozoic Calc-Alkaline Granitic Batholiths of the Sierra Nevada and Peninsular Ranges, California. *Journal of Geophysical Research*, 86(B11): 10470–10488. https://doi.org/10.1029/jb086ib11p10470

Duarte, B. P., Valente, S. C., Heilbron, M., et al., 2004. Petrogenesis of the Orthogneisses of the Mantiqueira Complex, Central Ribeira Belt, SE Brazil: An Archaean to Palaeoproterozoic Basement Unit Reworked During the Pan-African Orogeny. *Gondwana Research*, 7(2): 437–450. https://doi.org/10.1016/s1342-937x(05)70795-4

Ebadi, A., Johannes, W., 1991. Beginning of Melting and Composition of First Melts in the System Qz-Ab-Or-$H_2O$-$CO_2$. *Contributions to Mineralogy and Petrology*, 106(3): 286–295. https://doi.org/10.1007/bf00324558

Elhlou, S., Belousova, E., Griffin, W. L., et al., 2006. Trace Element and Isotopic Composition of GJ-Red Zircon Standard by Laser Ablation. *Geochimica et Cosmochimica Acta*, 70(18): A158. https://doi.org/10.1016/j.gca.2006.06.1383

Farina, F., Stevens, G., Villaros, A., 2012. Multi-Batch, Incremental Assembly of a Dynamic Magma Chamber: The Case of the Peninsula Pluton Granite (Cape Granite Suite, South Africa). *Mineralogy and Petrology*, 106(3/4): 193–216. https://doi.org/10.1007/s00710-012-0224-8

Frost, B. R., Barnes, C. G., Collins, W. J., et al., 2001. A Geochemical Classification for Granitic Rocks. *Journal of Petrology*, 42(11): 2033–2048. https://doi.org/10.1093/petrology/42.11.2033

Heilbron, M., Duarte, B. P., Valeriano, C. M., et al., 2010. Evolution of Reworked Paleoproterozoic Basement Rocks within the Ribeira Belt (Neoproterozoic), SE-Brazil, Based on U-Pb Geochronology: Implications for Paleogeographic Reconstructions of the São Francisco-Congo Paleocontinent. *Precambrian Research*, 178(1–4): 136–148. https://doi.org/10.1016/j.precamres.2010.02.002

Heilbron, M., Ribeiro, A., Valeriano, C. M., et al., 2017. The Ribeira Belt. In: Heilbron, M., Cordani, U., Alkmim, F., eds., São Francisco Craton, Eastern Brazil: Tectonic Genealogy of a Miniature Continent (Regional Geology Reviews). Springer. 277–302

Higgins, M. D., 1999. Origin of Megacrysts in Granitoids by Textural Coarsening; A Crystal Size Distribution (CSD) Study of Microcline in the Cathedral Peak Granodiorite, Sierra Nevada, California. In: Fernandez, C., Castro, A., Vigneresse, J. L., eds., Understanding Granites: Integrating Modern and Classical Techniques. *Geological Society Special*, 168: 207–219

Holtz, F., Barbey, P., Johannes, W., et al., 1989. Composition and Temperature at the Minimum Point in the Qz-Ab-Or System for $H_2O$-Undersaturated Conditions: Experimental Investigation. *Terra Cognita*, 1: 271–272

Holtz, F., Johannes, W., 1991. Genesis of Peraluminous Granites: I. Experimental Investigation of Melt Composition at 3 and 5 kb and Various $H_2O$ Activities. *Journal of Petrology*, 32(5): 935–958. https://doi.org/10.1093/petrology/32.5.935

Holtz, F., Johannes, W., Tamic, N., et al., 2001. Maximum and Minimum Water Contents of Granitic Melts Generated in the Crust: A Reevaluation and Implications. *Lithos*, 56(1): 1–14. https://doi.org/10.1016/s0024-4937(00)00056-6

Johannes, W., Holtz, F., 1996. Petrogenesis and Experimental Petrology of Granitic Rocks. Springer, Berlin. 335

Johnson, B. R., Glazner, A. F., 2010. Formation of K-Feldspar Megacrysts in Granodioritic Plutons by Thermal Cycling and Late-Stage Textural Coarsening. *Contributions to Mineralogy and Petrology*, 159(5): 599–619. https://doi.org/10.1007/s00410-009-0444-z

Kösler, J., Fonneland, H., Sylvester, P., et al., 2002. U-Pb Dating of Detrital Zircons for Sediment Provenance Studies—A Comparison of Laser Ablation ICPMS and SIMS Techniques. *Chemical Geology*, 182(2): 605–618. https://doi.org/10.1016/s0009-2541(01)00341-2

Ludwig, K. R., 2001. Squid (1.13b): A User's Manual. Berkeley Geochronology Center Special Publication, Berkeley. 2

Ludwig, K. R., 2003. User's Manual for ISOPLOT 3.00: A Geochronological Toolkit for Microsoft Excel. Berkeley Geochronological Center Special Publication, Berkeley. 4: 70

Luth, W. C., Jahns, R. H., Tuttle, O. F., 1964. The Granite System at Pressure of 4 to 10 Kilobars. *Journal of Geophysical Research*, 69: 759–773

Maaløe, S., Wyllie, P. J., 1975. Water Content of a Granite Magma Deduced from the Sequence of Crystallization Determined Experimentally with Water-Undersaturated Conditions. *Contributions to Mineralogy and Petrology*, 52(3): 175–191. https://doi.org/10.1007/bf00457293

Middlemost, E. A. K., 1985. Magmas and Magmatic Rocks. Logman, London. 87–88

Miller, C. F., Furbish, D. J., Walker, B. A., et al., 2011. Growth of Plutons by Incremental Emplacement of Sheets in Crystal-Rich Host: Evidence from Miocene Intrusions of the Colorado River Region, Nevada, USA. *Tectonophysics*, 500(1): 65–77. https://doi.org/10.1016/j.tecto.2009.07.011

Mills, R. D., Glazner, A. F., 2013. Experimental Study on the Effects of Temperature Cycling on Coarsening of Plagioclase and Olivine in an Alkali Basalt. *Contributions to Mineralogy and Petrology*, 166(1): 97–111. https://doi.org/10.1007/s00410-013-0867-4

Moreira, H., Seixas, L., Storey, C., et al., 2018. Evolution of Siderian Juvenile Crust to Rhyacian High Ba-Sr Magmatism in the Mineiro Belt, Southern São Francisco Craton. *Geoscience Frontiers*, 9(4): 977–995. https://doi.org/10.1016/j.gsf.2018.01.009

Moyen, J.-F., Laurent, O., 2018. Archaean Tectonic Systems: A View from Igneous Rocks. *Lithos*, 302/303: 99–125. https://doi.org/10.1016/j.lithos.2017.11.038

Nakamura, N., 1974. Determination of REE, Ba, Fe, Mg, Na and K in Carbonaceous and Ordinary Chondrites. *Geochimica et Cosmochimica Acta*, 38(5): 757–775. https://doi.org/10.1016/0016-7037(74)90149-5

Noce, C. M., Pedrosa-Soares, A. C., Silva, L. C., et al., 2007. Evolution of Polycyclic Basement Complexes in the Araçuaí orogen, Based on U-Pb SHRIMP Data: Implication of Brazil-Africa Links in Paleoproterozoic Time. *Precambrian Research*, 159(1/2): 60–78. https://doi.org/10.1016/j.precamres.2007.06.001

Nockolds, S. R., 1947. The Relation between Chemical Composition and Paragenesis in the Biotite Micas of Igneous Rocks. *American Journal of Science*, 245: 401–420. https://doi.org/10.2475/ajs.245.7.401

Patiño Douce, A. E., Beard, J. S., 1995. Dehydration Melting of Biotite Gneiss and Quartz Amphibolite from 3 to 15 kbar. *Journal of Petrology*, 36(3): 707–738. https://doi.org/10.1093/petrology/36.3.707

Patiño Douce, A. E., McCarthy, T. C., 1998. Melting of Continental Rocks During Continental Collision and Subduction. In: Hacker, B., Liou, J. G., eds., When Continents Collides: Geodynamics and Geochemistry of Ultra-High Pressure Rocks. Kluwer Academic Publisher, Dordrecht. 27–55

Pearce J. A., Harris, N. B. W., Tindle, A. G., 1984. Trace Elements Discrimination Diagrams for the Tectonic Interpretation of Granite Rocks. *Journal of Petrology*, 25(4): 956–983. https://doi.org/10.1093/petrology/25.4.956

Pearce, J., 1996. Sources and Settings of Granitic Rocks. *Episodes*, 19(4): 120–125

Peccerillo, A., Taylor, S. R., 1976. Geochemistry of Eocene Calc-Alkaline Volcanic Rocks from the Kastamonu Area, Northern Turkey. *Contributions to Mineralogy and Petrology*, 58(1): 63–81. https://doi.org/10.1007/bf00384745

Petronilho, L. A., 2009. O Método Sm-Nd no CPGeo-IGc-USP: Procedimentos Analíticos Atualmente em Rotina. Simpósio 45 anos de Geocronologia no Brasil, Instituto de Geociências, USP. Boletim de Resumos Expandidos, São Paulo. 116–118 (in Portuguese)

Pimentel, M. M., Charnley, N., 1991. Intracrustal REE Fractionation and Implications for SMND Model Age Calculations in Late-Stage Granitic Rocks: An Example from Central Brazil. *Chemical Geology: Isotope Geoscience Section*, 86(2): 123–138. https://doi.org/10.1016/0168-9622(91)90058-5

Ribeiro, A., Teixeira, W., Dussin, I. A., et al., 2013. U-Pb LA-ICP-MS Detrital Zircon Ages of the São João del Rei and Carandaí Basins: New Evidence of Intermittent Proterozoic Rifting in the São Francisco Paleocontinent. *Gondwana Research*, 24(2): 713–726. https://doi.org/10.1016/j.gr.2012.12.016

Roberts, M. P., Clemens, J. D., 1993. Origin of High-Potassium, Talc-Alkaline, I-Type Granitoids. *Geology*, 21(9): 825–828. https://doi.org/10.1130/0091-7613(1993)021<0825:oohpta>2.3.co;2

Sato, K., Tassinari, C. C. G., Kawashita, K., et al., 1995. O Método Geocronológico Sm-Nd no IG/USP e Suas Aplicações. *Anais da Academia Brasileira de Ciências*, 67: 313–336

Sato, K., Basei, M. A. S., Siga Junior, O., et al., 2010. *In situ* U-Th-Pb Isotopic Analyses by Excimer Laser Ablation/ICP-MS on Brazilian Megacrystal Xenotime: First Results on U-Pb Isoptes at CPGeo-IGC-USP. VII SSAGI-South American Simposium on Isotope Geology, Brasília. 349–352

Sato, K., Tassinari, C. C. G., Basei, M. A. S., et al., 2014. Sensitive High Resolution Ion Microprobe (SHRIMP IIe/MC) of the Institute of Geosciences of the University of São Paulo, Brazil: Analytical Method and First Results. *Geologia USP, Série Científica*, 14(3): 3–18

Sawyer, E. W., Cesare, B., Brown, M., 2011. When the Continental Crust Melts. *Elements*, 7(4): 229–234. https://doi.org/10.2113/gselements.7.4.229

Seixas, L. A. R., David, J., Stevenson, R., 2012. Geochemistry, Nd Isotopes and U-Pb Geochronology of a 2 350 Ma TTG Suite, Minas Gerais, Brazil: Implications for the Crustal Evolution of the Southern São Francisco Craton. *Precambrian Research*, 196/197: 61–80. https://doi.org/10.1016/j.precamres.2011.11.002

Seixas, L. A. R., Bardintzeff, J. M., Stevenson, R., et al., 2013. Petrology of the High-Mg Tonalites and Dioritic Enclaves of the ca. 2 130 Ma Alto Maranhão Suite: Evidence for a Major Juvenile Crustal Addition Event during the Rhyacian Orogenesis, Mineiro Belt, Southeast Brazil. *Precambrian Research*, 238: 18–41. https://doi.org/10.1016/j.precamres.2013.09.015

Silva, M. M., Holtz, F., Namur, O., 2017. Crystallization Experiments in Rhyolitic Systems: The Effect of Temperature Cycling and Starting Material on Crystal Size Distribution. *American Mineralogist*, 102(11): 2284–2294. https://doi.org/10.2138/am-2017-5981

Silva, M. M., Ávila, C. A., Barbosa, N. S., et al., 2020. Caracterização do Ortognaisse Brejo Alegre e sua Inserção no Contexto Evolutivo do Cinturão Mineiro, Cráton do São Francisco. *Anuário do Instituto de Geociências— UFRJ*, 43(2): 252–269 (in Portuguese with English Abstract)

Stacey, J. S., Kramers, J. D., 1975. Approximation of Terrestrial Lead Isotope Evolutionby a Two Stage Model. *Earth and Planetary Science Letters*, 26(2): 207–221. https://doi.org/10.1016/0012-821x(75)90088-6

Teixeira, W., Ávila, C. A., Nunes, L. C., 2008. Nd-Sr Isotopic Geochemistry and Geochronology of the Fé Granitic Gneiss and Lajedo Granodirite: Implications for Paleoproterozoic Evolution of the Mineiro Belt, Southern São Francisco Craton, Brazil. *Revista do Instituto de Geociências*, 8: 53–74

Teixeira, W., Ávila, C. A., Dussin, I. A., et al., 2015. A Juvenile Accretion Episode (2.35–2.32 Ga) in the Mineiro Belt and Its Role to the Minas Accretionary Orogeny: Zircon U-Pb-Hf and Geochemical Evidences. *Precambrian Research*, 256(4): 148–169. https://doi.org/10.1016/j.precamres.2014.11.009

Thompson, A. B., Connolly, J. A. D., 1995. Melting of the Continental Crust: Some Thermal and Petrological Constraints on Anatexis in Continental

Collision Zones and Other Tectonic Settings. *Journal of Geophysical Research*, 100(B8): 15565–15579. https://doi.org/10.1029/95jb00191

Tuttle, O. F., Bowen, N. L., 1958. Origin of Granite in the Light of Experimental Studies in the System NaAlSi$_3$O$_8$-KA1Si$_3$O$_8$-SiO$_2$-H$_2$O. *Geological Society of America Memoir*, 74: 1–154. https://doi.org/10.1130/mem74

Vasconcelos, F. F., Ávila, C. A., Neumann, R., et al., 2017. Ortognaisse Morro do Resende: Mineralogia, Petrografia, Geoquímica e Geocronologia. *Geologia USP. Série Científica*, 17: 143–164

Vernon, R. H., Paterson, S. R., 2008. How Late are K-Feldspar Megacrysts in Granites? *Lithos*, 104(1–4): 327–336. https://doi.org/10.1016/j.lithos.2008.01.001

Villaseca, C., Barbero, L., Herreros, V., 1998. A Re-Examination of the Typology of Peraluminous Granite Types in Intracontinental Orogenic Belts. *Transactions of the Royal Society of Edinburgh, Earth Sciences*,

89(2): 113–119. https://doi.org/10.1017/s0263593300007045

Watson, E. B., Harrison, T. M., 1983. Zircon Saturation Revisited: Temperature and Composition Effects in a Variety of Crustal Magma Types. *Earth Planetary Science Letters*, 64(3): 295–304. https://doi.org/10.1016/0012-821x(83)90211-x

Weaver, B. L., Tarney, J., 1984. Empirical Approach to Estimating the Composition of the Continental Crust. *Nature*, 310(5978): 575–577. https://doi.org/10.1038/310575a0

Weinberg, R. F., Hasalová, P., 2015. Water-Fluxed Melting of the Continental Crust: A Review. *Lithos*, 212–215: 158–188. https://doi.org/10.1016/j.lithos.2014.08.021

Whitney, J. A., 1988. The Origin of Granite: The Role and Source of Water in the Evolution of Granitic Magmas. *Geological Society of America Bulletin*, 100(12): 1886–1897. https://doi.org/10.1130/0016-7606(1988)100<1886:toogtr>2.3.co;2